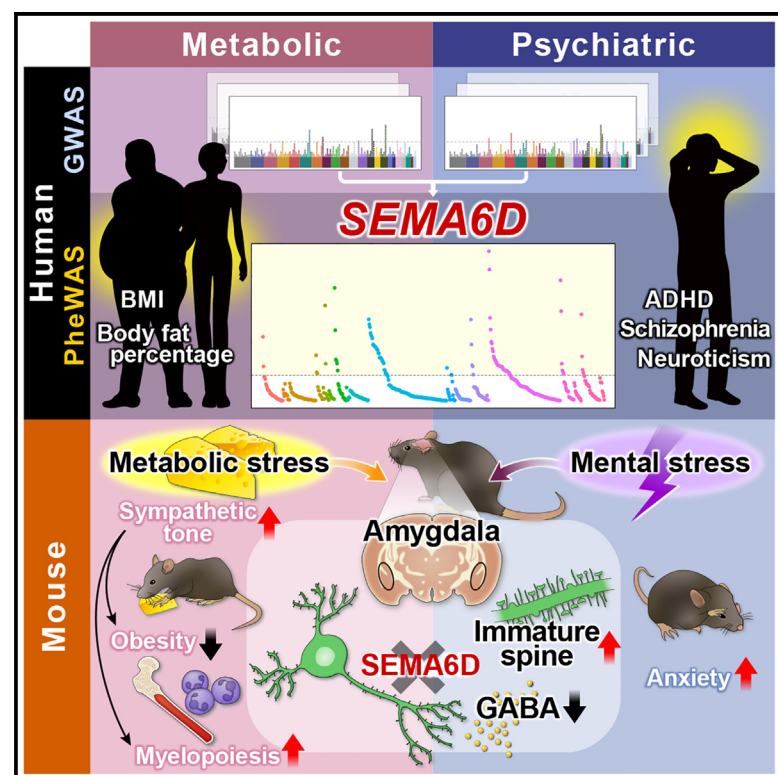| Title	Semaphorin 6D tunes amygdalar circuits for emotional, metabolic, and inflammatory outputs
Author(s)	Nakanishi, Yoshimitsu; Izumi, Mayuko; Matsushita, Hiroaki et al.
Citation	Neuron. 2024, 112(17), p. 2955-2972.e9
Version Type	VoR
URL	https://hdl.handle.net/11094/98345
rights	This article is licensed under a Creative Commons Attribution 4.0 International License.
Note	

Semaphorin 6D tunes amygdalar circuits for emotional, metabolic, and inflammatory outputs

Graphical abstract

Highlights

- *SEMA6D* is a pleiotropic gene for psychiatric and metabolic traits in human

- Loss of SEMA6D elevates anxiety, mitigates obesity, and enhances myelopoiesis

- Amygdalar SEMA6D regulates anxiogenic and autonomic responses

- SEMA6D controls synaptic maturation and GABAergic transmission in the amygdala

Authors

Yoshimitsu Nakanishi, Mayuko Izumi, Hiroaki Matsushita, ..., Shoichi Shimada, Sujin Kang, Atsushi Kumanogoh

Correspondence

kang@ifrec.osaka-u.ac.jp (S.K.), kumanogo@ imed3.med.osaka-u.ac.jp (A.K.)

In brief

Nakanishi et al. reveal that semaphorin 6D signaling maintains synaptic homeostasis and regulates GABAergic transmission in the amygdala, thereby coordinating emotional, metabolic, and inflammatory responses under stress conditions.

CellPress

Article

Semaphorin 6D tunes amygdalar circuits for emotional, metabolic, and inflammatory outputs

Yoshimitsu Nakanishi,[1,2,3,4,18] Mayuko Izumi,[1,2,3,4,18] Hiroaki Matsushita,[3,5] Yoshihisa Koyama,[4,6,7] Diego Diez,[8]
Hyota Takamatsu,[1,2] Shohei Koyama,[1,2] Masayuki Nishide,[1,2] Maiko Naito,[1,2] Yumiko Mizuno,[1,2] Yuta Yamaguchi,[1,2]
Tomoki Mae,[1] Yu Noda,[1] Kamon Nakaya,[1] Satoshi Nojima,[9] Fuminori Sugihara,[10] Daisuke Okuzaki,[4,11,12,15,16]
Masahito Ikawa,[13,15,17] Shoichi Shimada,[6,7] Sujin Kang,[14,15,*] and Atsushi Kumanogoh[1,2,4,15,16,17,19,*]

[1]Department of Respiratory Medicine and Clinical Immunology, Graduate School of Medicine, Osaka University, Osaka 565-0871, Japan
[2]Department of Immunopathology, World Premier International Research Center Initiative Immunology Frontier Research Center
(WPI-IFReC), Osaka University, Osaka 565-0871, Japan
[3]Department of Advanced Clinical and Translational Immunology, Graduate School of Medicine, Osaka University, Osaka 565-0871, Japan
[4]Integrated Frontier Research for Medical Science Division, Institute for Open and Transdisciplinary Research Initiatives (OTRI), Osaka
University, Osaka 565-0871, Japan
[5]Discovery Pharmacology Department, Research Division, Chugai Pharmaceutical Co. Ltd., Kanagawa 247-8530, Japan
[6]Department of Neuroscience and Cell Biology, Graduate School of Medicine, Osaka University, Osaka 565-0871, Japan
[7]Addiction Research Unit, Osaka Psychiatric Research Center, Osaka Psychiatric Medical Center, Osaka 541-8567, Japan
[8]Quantitative Immunology Research Unit, WPI-IFReC, Osaka University, Osaka 565-0871, Japan
[9]Department of Pathology, Graduate School of Medicine, Osaka University, Osaka 565-0871, Japan
[10]Laboratory of Biofunctional Imaging, WPI-IFReC, Osaka University, Osaka 565-0871, Japan
[11]Laboratory of Human Immunology (Single Cell Genomics), WPI-IFReC, Osaka University, Osaka 565-0871, Japan
[12]Genome Information Research Center, Research Institute for Microbial Diseases (RIMD), Osaka University, Osaka 565-0871, Japan
[13]Department of Experimental Genome Research, RIMD, Osaka University, Osaka 565-0871, Japan
[14]Laboratory of Immune Regulation, WPI-IFReC, Osaka University, Osaka 565-0871, Japan
[15]Center for Infectious Diseases for Education and Research (CiDER), Osaka University, Osaka 565-0871, Japan
[16]Japan Agency for Medical Research and Development—Core Research for Evolutional Science and Technology (AMED–CREST), Osaka
University, Osaka 565-0871, Japan
[17]Center for Advanced Modalities and DDS (CAMaD), Osaka University, Osaka 565-0871, Japan
[18]These authors contributed equally
[19]Lead contact
*Correspondence: kang@ifrec.osaka-u.ac.jp (S.K.), kumanogo@imed3.med.osaka-u.ac.jp (A.K.)
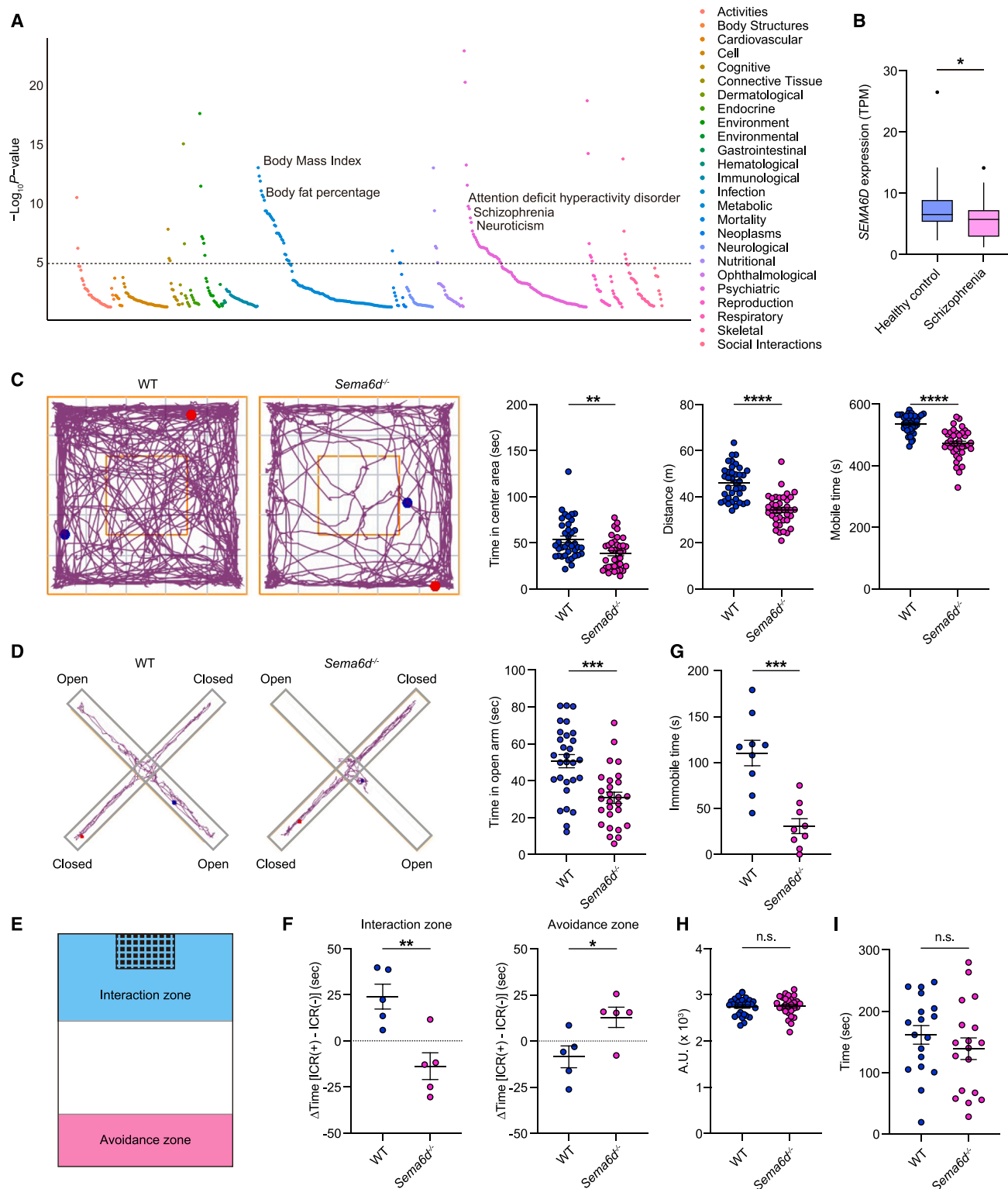https://doi.org/10.1016/j.neuron.2024.06.017

SUMMARY

Regulated neural-metabolic-inflammatory responses are essential for maintaining physiological homeostasis. However, the molecular machinery that coordinates neural, metabolic, and inflammatory responses is largely unknown. Here, we show that semaphorin 6D (SEMA6D) coordinates anxiogenic, metabolic, and inflammatory outputs from the amygdala by maintaining synaptic homeostasis. Using genome-wide approaches, we identify *SEMA6D* as a pleiotropic gene for both psychiatric and metabolic traits in human. *Sema6d* deficiency increases anxiety in mice. When fed a high-fat diet, *Sema6d*^{−/−} mice display attenuated obesity and enhanced myelopoiesis compared with control mice due to higher sympathetic activity via the β3-adrenergic receptor. Genetic manipulation and spatial and single-nucleus transcriptomics reveal that SEMA6D in amygdalar interneurons is responsible for regulating anxiogenic and autonomic responses. Mechanistically, SEMA6D is required for synaptic maturation and γ-aminobutyric acid transmission. These results demonstrate that SEMA6D is important for the normal functioning of the neural circuits in the amygdala, coupling emotional, metabolic, and inflammatory responses.

INTRODUCTION

Mutual interactions among the neural, metabolic, and immune systems are physiologically and pathologically pivotal for tissue homeostasis. Deficiencies in these interactions frequently result in overlapping pathologies across a spectrum of human diseases, including psychiatric, metabolic, and inflammatory disorders.[1–4] Several lines of evidence suggest that the brain, as a central regulator of the body, receives signals from peripheral tissues and establishes coordinated neural-metabolic-inflammatory responses.[5–7] However, the molecular machinery that coordinates neural,

Figure 1. Loss of *Sema6d* increases anxiety

(A) Phenome-wide association of *SEMA6D* polymorphisms across 4,756 GWASs from the GWAS Atlas.

(B) *SEMA6D* mRNA expression in the amygdala from patients with schizophrenia compared with controls in the PRJNA379666 dataset. TPM, transcripts per kilobase million. Boxes denote the interquartile range (IQR). The median is shown as horizontal bars. Whiskers extend to 1.5 times the IQR. Outliers are shown as individual points. Healthy controls, $n = 24$; patients with schizophrenia, $n = 22$.

(legend continued on next page)

metabolic, and inflammatory outputs from the brain is largely unknown.

Neural circuit formation relies on multiple processes, such as axonal projection, synaptic maturation, and synaptic pruning.[8] Various attractive and repulsive axon guidance cues orchestrate these processes. Semaphorins are one of the largest families of repulsive axonal guidance molecules, regulating early processes of neural circuit formation, such as axonal projection, and later neural developmental processes, such as neurite pruning.[9,10] Semaphorin 6D (SEMA6D), a transmembrane-type semaphorin, exerts multiple biological effects, including axon guidance,[11,12] cardiac development,[13,14] bone remodeling,[15] and immune responses.[16,17] As an axon guidance molecule, SEMA6D is involved in the formation of the optic chiasm[11] and the elimination of corticomotor neuronal connections.[12] Furthermore, genetic variants of SEMA6D are associated with susceptibility to schizophrenia, attention-deficit hyperactivity disorder, and neuroticism.[18–20] In addition, we have previously reported that SEMA6D-Plexin-A4 (PLXNA4) signaling promotes anti-inflammatory macrophage polarization via enhanced intracellular lipid metabolism.[17] However, despite the growing appreciation for the roles of SEMA6D in neural and immuno-metabolic processes, it remains to be determined whether SEMA6D plays key roles in coordinating neural, metabolic, and inflammatory outputs from the brain.

This study aimed to investigate the interactions among neural, metabolic, and inflammatory responses using genome-wide approaches, genetic manipulation, and spatial and single-nucleus transcriptomics, thereby focusing on the contribution of SEMA6D in the amygdala. We presented SEMA6D as a pleiotropic gene for psychiatric and metabolic traits through genome-wide analyses; amygdala SEMA6D functions as a common hub for anxiogenic, metabolic, and hematopoietic responses by supporting synaptic maturation and γ-aminobutyric acid (GABA) transmission. Our study could provide insight into developing strategies to treat disorders related to the dysregulation of emotions, metabolism, and inflammation by targeting SEMA6D.

RESULTS

SEMA6D is a pleiotropic gene of both psychiatric and metabolic traits in human

To reveal the existence of shared genetic factors for neural and metabolic responses, we first examined the genetic correlation between psychiatric and metabolic traits using cross-trait linkage disequilibrium score regression (LDSC).[21] We computed pairwise genetic correlations (r_g) among 16 metabolic and 18 psychiatric traits from the genome-wide association study (GWAS) atlas.[22] We found a significant genetic correlation between psychiatric and metabolic traits, suggesting the presence of shared biological pathways across multiple traits (Figure S1A). This observation was consistent with previous GWAS meta-analysis, which revealed enriched expression of body mass index (BMI)-associated genes in the brain.[5] We next investigated pleiotropic genes associated with psychiatric and metabolic traits and identified 59 potential pleiotropic genes, including neurexin 1 (NRXN1), erb-b2 receptor tyrosine kinase 4 (ERBB4), roundabout guidance receptor 2 (ROBO2), cell adhesion molecule 2 (CADM2), myocyte enhancer factor 2C (MEF2C), teneurin transmembrane protein 2 (TENM2), brain-derived neurotrophic factor (BDNF), transcription factor 4 (TCF4), and SEMA6D (Figure S1B). Given the multifaceted roles of semaphorins in neural development, we further investigated the pleiotropic effects of SEMA6D variants. To pathophysiologically annotate the genetic variants of SEMA6D, we performed a phenome-wide association study of the SEMA6D variant across 4,756 GWASs from the GWAS atlas[22] and identified its significant effects on psychiatric (schizophrenia, attention-deficit hyperactivity disorder, and neuroticism) and metabolic traits (BMI and fat percentage) (Figure 1A). In addition, ribonucleic acid sequencing (RNA-seq) of postmortem brain tissues showed the downregulation of SEMA6D in the amygdala of patients with schizophrenia compared with that of healthy controls (Figure 1B), suggesting that loss of function of SEMA6D is associated with schizophrenia.

Sema6d$^{-/-}$ mice show increased anxiety-like behavior
Based on these findings, we investigated whether Sema6d$^{-/-}$ mice exhibit behavioral alterations. We performed comprehensive behavioral phenotyping to determine the role of SEMA6D in anxiety-like, depression-like, and social behavior and sensorimotor functions. The open-field (OF) test evaluates the tendency of mice to avoid open spaces (central zone) and remain close to the walls, which is an indicator of anxiety-like behavior.[23,24] Sema6d$^{-/-}$ mice were less inclined to explore the central area of the OF test chamber compared with wild-type (WT) mice, and the total mobile distance and exploration time were significantly decreased for Sema6d$^{-/-}$ mice during the test (Figure 1C). In the elevated plus maze (EPM) test, mice naturally avoid unprotected open arms and favor darker and safer enclosed arms, which reflect the anxiety state.[23,25] Sema6d$^{-/-}$ mice exhibited significantly decreased exploration times in the open arms of the EPM test compared with WT mice (Figure 1D). Moreover,

(C) Representative tracks, time spent in the center, travel distance, and mobile time of wild-type (WT) and Sema6d$^{-/-}$ mice in the open-field test (OFT). n = 38.

(D) Representative tracks and time spent in the open arm in the elevated plus maze (EPM) test. n = 27–29.

(E) Definitions of social interaction and social avoidance zones (blue and pink rectangles, respectively).

(F) Levels of social interaction and social avoidance. The differences between the durations of the interaction or avoidance zone with and without ICR mice (ΔTime [ICR(+) − ICR(−)]) were analyzed. n = 5.
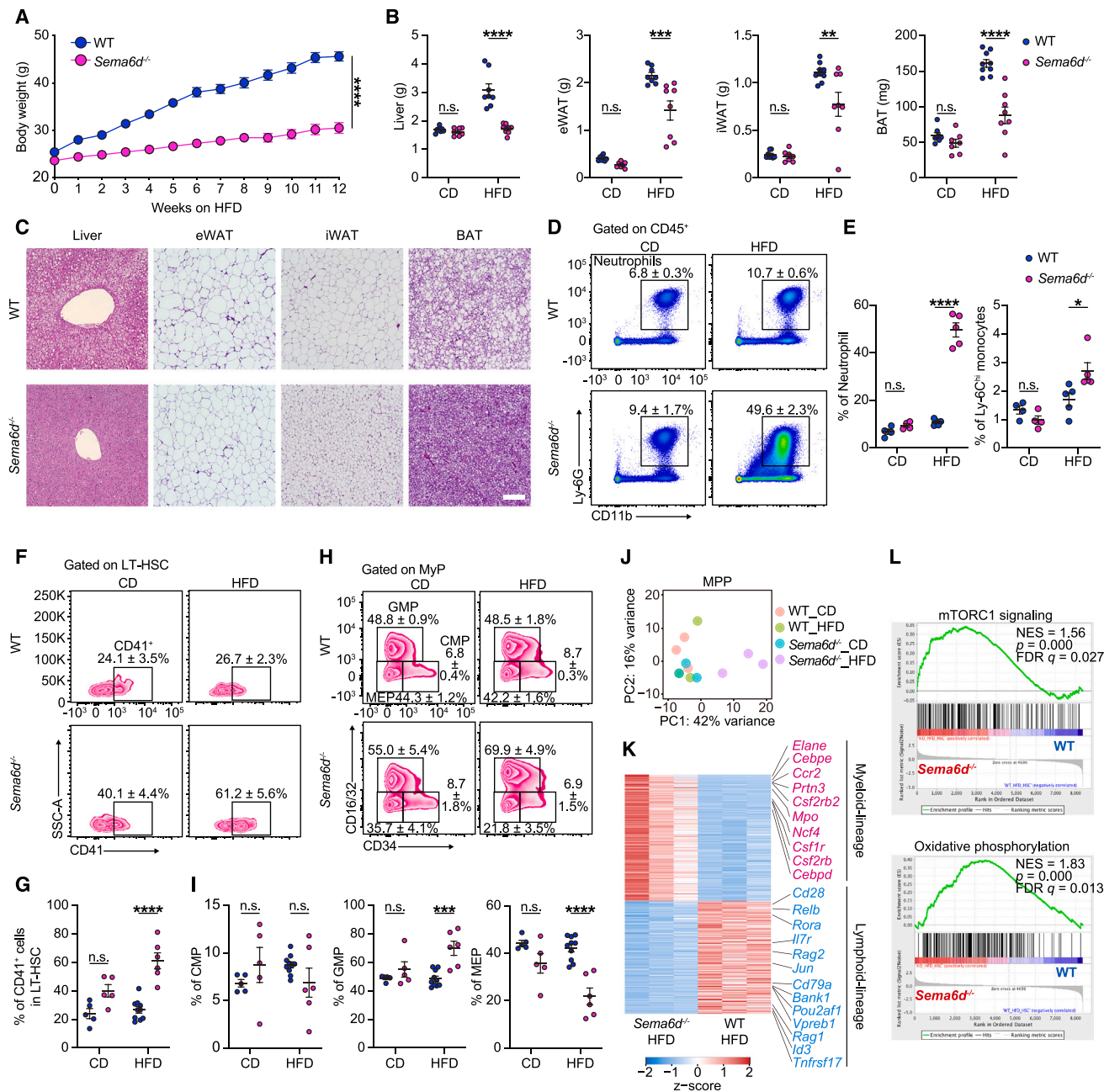
(G) Performance in the forced swimming test. n = 9.

(H) Spontaneous locomotor activities. n = 28.

(I) The latency time to fall in the rotarod test. n = 18.

Data are presented as mean ± SEM except for (B). *$p < 0.05$, **$p < 0.01$, ***$p < 0.001$, ****$p < 0.0001$. n.s., not significant. Mann-Whitney test (B); unpaired two-tailed Student's t tests (C, D, and F–I).

See also Figure S1.

Figure 2. HFD-fed *Sema6d*⁻/⁻ mice exhibit resistance to obesity, followed by enhanced myelopoiesis

WT and *Sema6d*⁻/⁻ mice were fed CD or HFD for 12 weeks.

(A) Body weights. $n = 8$.

(B) Liver, epididymal white adipose tissue (eWAT), inguinal white adipose tissue (iWAT), and brown adipose tissue (BAT) weights. $n = 7–8$.

(C) Representative hematoxylin and eosin (H&E) staining images of the liver, eWAT, iWAT, and BAT of HFD-fed WT and *Sema6d*⁻/⁻ mice. Scale bars, 200 μm.

(D) Representative fluorescence-activated cell sorting (FACS) plots of neutrophils in the peripheral blood.

(E) Proportions of neutrophils and Ly-6Cʰⁱ monocytes in the peripheral blood. $n = 4–5$.

(F) Representative FACS plots of CD41⁺ LT-HSCs in the BM.

(G) The proportion of CD41⁺ LT-HSCs (versus total LT-HSCs) in the BM. $n = 5–10$.

(H) Representative FACS plots of MyP subpopulations in the BM.

(I) Proportions of CMPs, GMPs, and MEPs (versus MyPs) in the BM. $n = 5–10$.

(J) Principal component analysis of RNA-seq profiles of MPPs.

(K) Heatmap of differentially expressed genes ($|FC| \geq 2$, $p < 0.05$) in MPPs. Myeloid and lymphoid lineage-related genes are shown.

(legend continued on next page)

Sema6d^{−/−} mice used less time in the social interaction zone and more time in the social avoidance zone than the WT mice during the social interaction test (Figures 1E and 1F). We assessed behavioral immobility, termed ''learned helplessness,'' using the forced swimming test to evaluate depression-like behavior. *Sema6d*^{−/−} mice used less immobility time than the WT mice (Figure 1G), indicating that loss of SEMA6D induces anxiety-like behavior. Although these tests are sensitive to overall changes in locomotion, *Sema6d* deficiency did not affect spontaneous locomotion, motor coordination, and balance (Figures 1H and 1I). Taken together, these observations indicate that anxiety was elevated in *Sema6d*^{−/−} mice.

High-fat-diet-fed *Sema6d*^{−/−} mice exhibit resistance to obesity

Next, we investigated whether SEMA6D regulates systemic metabolism and inflammatory responses. Since metabolic disorders lead to the dysregulation of myelopoiesis and inflammatory responses,[26–29] we used a high-fat diet (HFD)-induced obesity model. *Sema6d*^{−/−} mice showed markedly reduced HFD-induced body mass gain compared with WT mice (Figure 2A), whereas the body weights of *Sema6d*^{−/−} mice were comparable to those of WT mice that were fed a control diet (CD) (Figure S2A). Lipid absorption and food consumption of *Sema6d*^{−/−} mice were similar to those of WT mice (Figures S2B and S2C). *Sema6d*^{−/−} mice exhibited lower liver, epididymal white adipose tissue (eWAT), inguinal WAT (iWAT), and brown adipose tissue (BAT) weights than WT mice under HFD conditions (Figure 2B). By contrast, no difference was observed between WT and *Sema6d*^{−/−} mice under CD conditions (Figure 2B). *Sema6d* deletion attenuated HFD-induced hepatic steatosis and adipocyte hypertrophy (Figures 2C and S2D). Likewise, plasma cholesterol levels in HFD-fed *Sema6d*^{−/−} mice were reduced compared with those in HFD-fed WT mice (Figure S2E). *Sema6d*^{−/−} mice exhibited lower HFD-induced glucose intolerance than WT mice (Figure S2F).

Given that SEMA6D is critical for the anti-inflammatory properties of macrophages,[17] we examined whether *Sema6d* deficiency affects the functions of adipose tissue macrophages (ATMs). Anti-inflammatory CD206^{+} ATMs maintain adipose tissue homeostasis, whereas pro-inflammatory CD11c^{+} ATMs expressing contribute to obesity pathogenesis.[30] Consistent with our previous study,[17] *Sema6d*^{−/−} mice showed a smaller proportion of anti-inflammatory CD206^{+} ATMs than WT mice with CD (Figure S2G). By contrast, HFD-fed *Sema6d*^{−/−} mice exhibited a higher proportion of anti-inflammatory CD206^{+} ATMs than HFD-fed WT mice (Figure S2G), suggesting that loss of SEMA6D-mediated anti-inflammatory properties of ATMs is irrelevant to metabolic abnormalities observed in HFD-fed *Sema6d*^{−/−} mice.

HFD-fed *Sema6d*^{−/−} mice exhibit enhanced myelopoiesis

Then, we investigated whether myelopoiesis was affected in HFD-fed *Sema6d*^{−/−} mice. HFD-fed *Sema6d*^{−/−} mice showed marked neutrophilia and monocytosis compared with HFD-fed WT mice (Figures 2D and 2E). To investigate hematopoietic adaptations in HFD-fed *Sema6d*^{−/−} mice, we analyzed hematopoietic progenitors (LSKs; Lin^{−}c-Kit^{+}Sca1^{+}), long-term hematopoietic stem cells (LT-HSCs; CD48^{−}CD150^{+} LSKs), multipotent progenitors (MPPs; CD48^{+}CD150^{−} LSKs), and myeloid progenitors (MyPs; Lin^{−}c-Kit^{+}Sca1^{−}) in the bone marrow (BM). In *Sema6d*^{−/−} mice, HFD increased the proportion of myeloid-biased CD41^{+} LT-HSCs (Figures 2F and 2G). Among MyPs of HFD-fed *Sema6d*^{−/−} mice, there was a high proportion of granulocyte/macrophage progenitors (GMPs; CD16/32^{+}CD34^{+} MyPs) and correspondingly a low proportion of megakaryocyte/erythrocyte progenitors (MEPs; CD16/32^{−}CD34^{−} MyPs) (Figures 2H and 2I), indicating enhanced myelopoiesis in *Sema6d*^{−/−} mice.

To characterize the molecular mechanism for enhanced myelopoiesis in HFD-fed *Sema6d*^{−/−} mice, we performed RNA-seq of HSCs (CD48^{−} LSKs) and MPPs from WT and *Sema6d*^{−/−} mice. Principal component analysis revealed that HFD-fed *Sema6d*^{−/−} MPPs exhibited a molecular signature distinct from CD-fed *Sema6d*^{−/−} MPPs (Figure 2J). By contrast, the expression pattern of HFD-fed WT MPPs resembled that of CD-fed WT MPPs (Figure 2J). Furthermore, the upregulation of myeloid lineage markers, including elastase, neutrophil expressed (*Elane*), colony-stimulating factor 2 receptor subunit beta (*Csf2rb*), and myeloperoxidase (*Mpo*), and the downregulation of lymphoid lineage markers, including interleukin 7 receptor (*Il7r*), V-set pre-B cell surrogate light-chain 1 (*Vpreb1*), recombination activating 1 (*Rag1*), and recombination activating 2 (*Rag2*), were also observed in MPPs from HFD-fed *Sema6d*^{−/−} mice (Figure 2K). Consistently, the myeloid lineage TCF CCAAT enhancer binding protein epsilon (*Cebpe*) was upregulated in MPPs from HFD-fed *Sema6d*^{−/−} mice, whereas the lymphoid lineage TCF RELB proto-oncogene, nuclear factor κB (NF-κB) subunit (*Relb*) was downregulated (Figure 2K). mTOR activation and the metabolic shift to oxidative phosphorylation promote HSC differentiation.[31] Consistently, gene set enrichment analysis[32,33] revealed a significant positive correlation between mTORC1 signaling and oxidative phosphorylation gene sets in HSCs of HFD-fed *Sema6d*^{−/−} mice (Figure 2L), suggesting that the *Sema6d*^{−/−} BM compartment is hypersensitive to HFD feeding by increasing myelopoiesis and reprogramming transcription in myeloid precursor cells. Therefore, SEMA6D plays a key role in metabolic and inflammatory regulation under HFD conditions.

SEMA6D suppresses sympathetic outflow and β3-adrenergic receptor signaling

Since the β3-adrenergic receptor (β3-AR) signaling promotes adipocyte lipolysis[34] and myelopoiesis,[35] we investigated whether abnormal systemic metabolism and myelopoiesis in *Sema6d*^{−/−} mice were due to increased sympathetic activity. We performed RNA-seq on WT and *Sema6d*^{−/−} epididymal adipocytes. HFD-fed *Sema6d*^{−/−} adipocytes exhibited a molecular

---

(L) Gene set enrichment analysis for mTORC1 signaling and oxidative phosphorylation in HSCs from WT and *Sema6d*^{−/−} mice treated with HFD. NES, normalized enrichment score. FDR, false discovery rate.

All data are presented as mean ± SEM. *$p < 0.05$, **$p < 0.01$, ***$p < 0.001$, ****$p < 0.0001$. n.s., not significant. Two-way ANOVA (A, B, E, G, and I).

See also Figure S2.
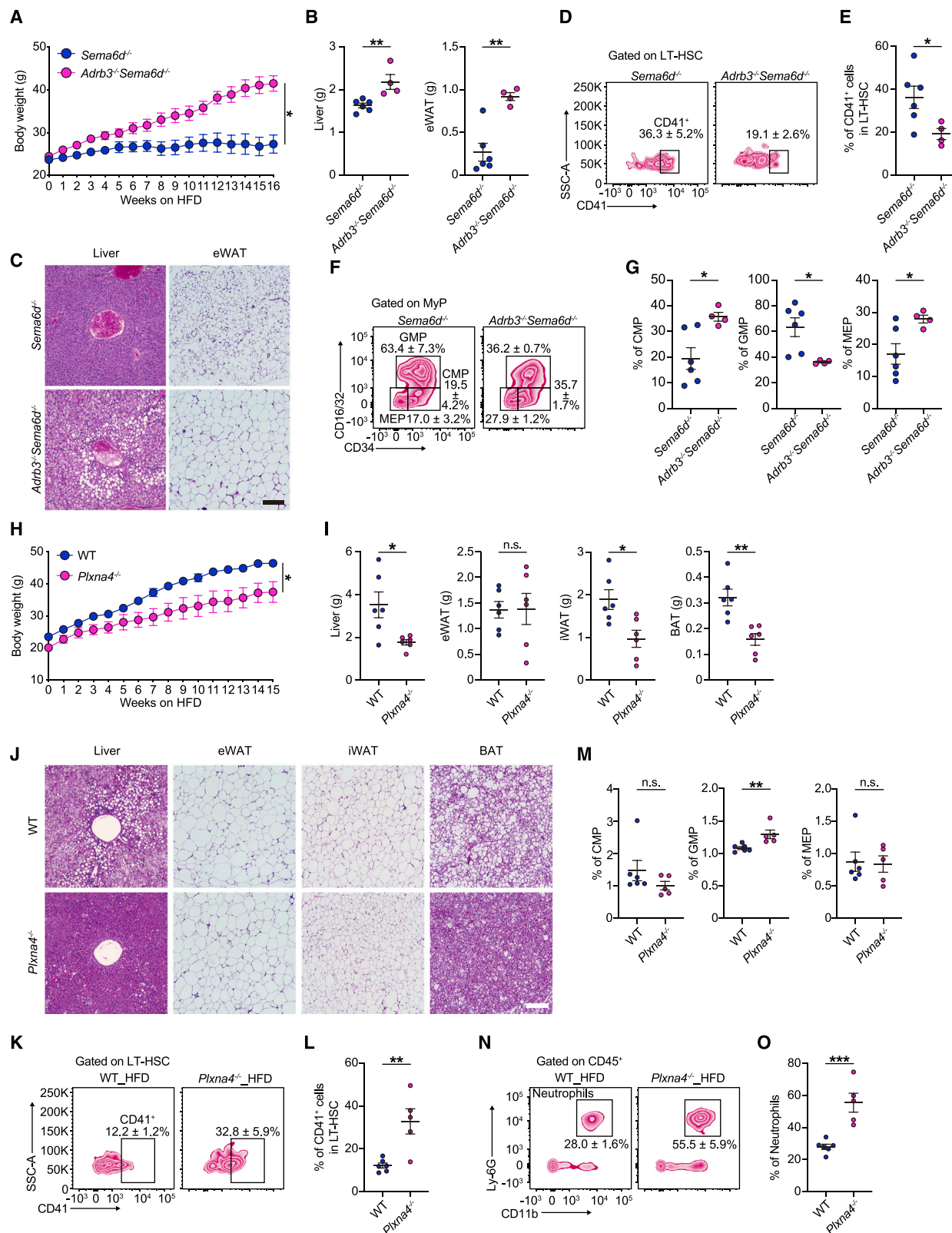
(legend on next page)

signature distinct from that of HFD-fed WT adipocytes, whereas the expression pattern of CD-fed *Sema6d*^{−/−} adipocytes was similar to that of CD-fed WT adipocytes (Figure S2H). We identified 2,081 differentially expressed genes (DEGs) in adipocytes from HFD-fed *Sema6d*^{−/−} mice compared with those from HFD-fed WT mice (Figures S2I and S2J). Pathway analysis based on the Kyoto Encyclopedia of Genes and Genomes database[36] demonstrated that the pathways involved in lipid metabolism, including lipolysis, were overrepresented in the upregulated genes (Figure S2K). By contrast, pathways involved in cell proliferation were overrepresented in the downregulated genes (Figure S2K), indicating that the deletion of *Sema6d* enhances catabolic responses in adipocytes under HFD conditions.

To determine whether abnormal β3-AR signaling is relevant to altered metabolism and hematopoiesis in *Sema6d*^{−/−} mice, we generated *Adrb3*^{−/−}*Sema6d*^{−/−} mice (Figures S2L–S2N). HFD-fed *Adrb3*^{−/−}*Sema6d*^{−/−} mice showed increased weight gain, hepatic steatosis, and eWAT hypertrophy compared with HFD-fed *Sema6d*^{−/−} mice (Figures 3A–3C). Moreover, *Adrb3* ablation ameliorated the myeloid skewing of LT-HSCs and MyPs (Figures 3D–3G). These results suggest that abnormal sympathetic outflow and β3-AR signaling were responsible for the metabolic and inflammatory phenotypes observed in HFD-fed *Sema6d*^{−/−} mice.

SEMA6D-PLXNA4 signaling axis couples systemic metabolism and myelopoiesis

Plexins function as semaphorin receptors that transduce signals in multiple cellular processes, either alone or in complex with neuropilins. Given that SEMA6D interacts with PLXNA4 in macrophages,[17] we investigated whether PLXNA4 was relevant to the metabolic and hematopoietic effects of SEMA6D. HFD-fed *Plxna4*^{−/−} mice exhibited reduced obesity, hepatic steatosis, and adipocyte hypertrophy compared with HFD-fed WT mice (Figures 3H–3J). Moreover, HFD treatment was associated with an enhanced myelopoiesis of *Plxna4*^{−/−} mice (Figures 3K–3O). Collectively, these data indicate that the SEMA6D-PLXNA4 signaling axis couples systemic metabolism and myelopoiesis.

SEMA6D expressed in non-hematopoietic cells regulates systemic metabolism and myelopoiesis

To determine whether SEMA6D expression in peripheral immune cells affects systemic metabolism and myelopoiesis, we generated BM chimeric mice by crisscross transplantation. We transferred either WT or *Sema6d*^{−/−} hematopoietic cells into lethally irradiated WT or *Sema6d*^{−/−} mice (WT→WT, WT→*Sema6d*^{−/−}, *Sema6d*^{−/−}→WT, *Sema6d*^{−/−}→*Sema6d*^{−/−}). HFD-induced obesity was significantly reduced in mice lacking *Sema6d* in all tissues (*Sema6d*^{−/−}→*Sema6d*^{−/−}) and in those with non-hematopoietic cells only (WT→*Sema6d*^{−/−}) (Figure 4A). By contrast, WT mice harboring *Sema6d*^{−/−} hematopoietic cells (*Sema6d*^{−/−}→WT) were vulnerable to HFD-induced obesity (Figure 4A). *Sema6d* deficiency in non-hematopoietic cells resulted in smaller liver, eWAT, iWAT, and BAT weights under HFD conditions (Figure 4B). Consistently, *Sema6d* deficiency in non-hematopoietic cells remarkably attenuated HFD-induced hepatic steatosis and adipocyte hypertrophy (Figures 4C–4E). Moreover, HFD-fed WT→*Sema6d*^{−/−} mice showed enhanced myelopoiesis compared with HFD-fed WT→WT mice, whereas HFD-fed *Sema6d*^{−/−}→WT mice did not exhibit such a phenotype (Figures 4F–4I). These results indicate that non-hematopoietic SEMA6D is responsible for metabolic and hematopoietic adaptations under HFD conditions.

SEMA6D in neurons orchestrates anxiogenic and autonomic responses

In addition to immune cells, other types of cells, including neural, endothelial, and mesenchymal cells, express SEMA6D. To determine the role of SEMA6D in endothelial and mesenchymal cells in systemic metabolism, we generated a knock-in mouse strain carrying a *loxP*-flanked (floxed) *Sema6d* allele (Figure S3A) and deleted *Sema6d* in endothelial and mesenchymal cells by breeding VEcad-Cre[ERT2] or Prx1-Cre mice with *Sema6d*^{fl/fl} mice (*Sema6d*[ΔVEcad] and *Sema6d*[ΔPrx1], respectively). As a result, *Sema6d*[ΔVEcad] and *Sema6d*[ΔPrx1] mice were vulnerable to HFD-induced obesity (Figures S3B–S3E), indicating that endothelial

---

Figure 3. SEMA6D-PLXNA4 signaling axis suppresses sympathetic outflow and β3-AR signaling

(A–G) *Sema6d*^{−/−} and *Adrb3*^{−/−}*Sema6d*^{−/−} mice were fed HFD for 16 weeks.

(A) Body weights. *n* = 4–6.

(B) Liver and eWAT weights. *n* = 4–6.

(C) Representative H&E-stained images of the liver and eWAT. Scale bars, 200 μm.

(D) Representative FACS plots of CD41^{+} LT-HSCs in the BM.

(E) The proportion of CD41^{+} LT-HSCs (versus total LT-HSCs) in the BM. *n* = 4–6.

(F) Representative FACS plots of MyP subpopulations in the BM.

(G) Proportions of CMPs, GMPs, and MEPs (versus MyPs) in the BM. *n* = 4–6.

(H–O) WT and *Plxna4*^{−/−} mice were fed HFD for 15 weeks.

(H) Body weights. *n* = 4.

(I) Liver, eWAT, iWAT, and BAT weights. *n* = 6.

(J) Representative H&E-stained images of the liver, eWAT, iWAT, and BAT. Scale bars, 200 μm.

(K) Representative FACS plots of CD41^{+} LT-HSCs in the BM.

(L) The proportion of CD41^{+} LT-HSCs (versus total LT-HSCs) in the BM. *n* = 5–6.

(M) Proportions of CMPs, GMPs, and MEPs in the BM. *n* = 5–6.

(N) Representative FACS plots identifying neutrophils in the peripheral blood.

(O) Proportions of neutrophils in the peripheral blood. *n* = 5–6.

All data are presented as mean ± SEM. *p < 0.05, **p < 0.01, ***p < 0.001. n.s., not significant. Two-way ANOVA (A and H); unpaired two-tailed Student's t tests (B, E, G, I, L, M, and O).

See also Figure S2.
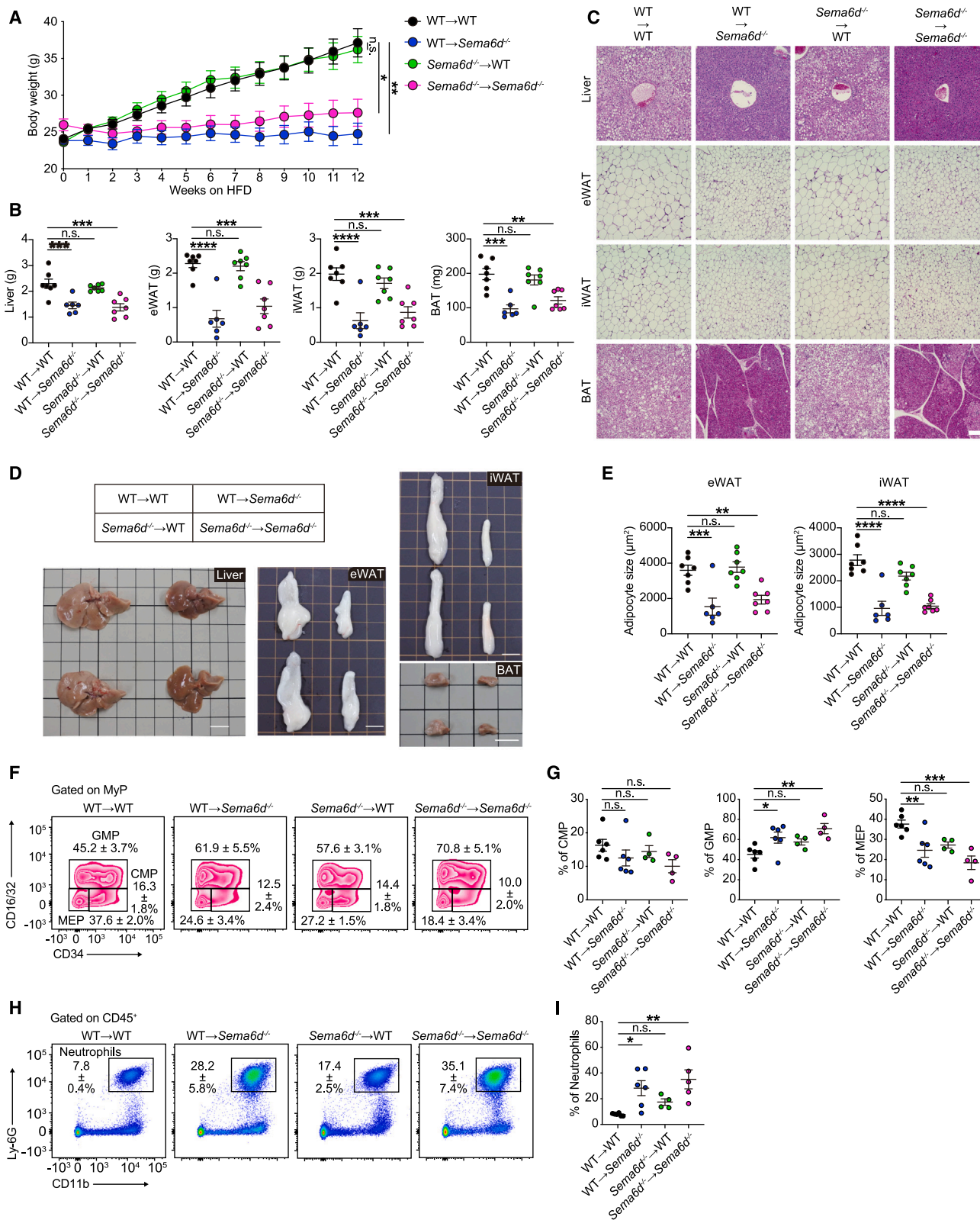
or mesenchymal SEMA6D is not involved in regulating systemic metabolism.

To define the role of SEMA6D in the brain, we generated _Sema6d_[IRES-Cre/+] mice with an internal ribosome entry site (IRES) and Cre recombinase in the _Sema6d_ 3′-UTR (Figure S4A). We crossed _Sema6d_[IRES-Cre/+] mice with a Cre-dependent ZsGreen1 reporter line, _Ai6_,[37] to visualize SEMA6D-expressing cells. Microscopic analysis revealed that SEMA6D was mainly expressed in neurons and microglia (MG) in the brain (Figure 5A). To determine the cellular source of SEMA6D responsible for regulating anxiogenic and autonomic responses, we deleted _Sema6d_ in neurons and MG by breeding Tau- or Cx3cr1-Cre mice with _Sema6d_[fl/fl] mice (_Sema6d_[ΔTau] and _Sema6d_[ΔCx3cr1], respectively) (Figures S4B and S4C). As was the case for _Sema6d_[−/−] mice, _Sema6d_[ΔTau] mice exhibited reduced exploration time in the OF test and decreased exploration time in the open arms of the EPM test compared with control mice, indicating that neural SEMA6D is responsible for regulating anxiety (Figures 5B and 5C). Since microglial inflammation affects behavioral responses,[38] we examined anxiogenic responses in _Sema6d_[ΔCx3cr1] mice. The OF and EPM tests revealed no altered anxiety-like behaviors in _Sema6d_[ΔCx3cr1] mice compared with control mice, indicating that microglial SEMA6D is irrelevant to behavioral regulation (Figures S4D and S4E). Furthermore, HFD-fed _Sema6d_[ΔTau] mice exhibited reduced obesity, hepatic steatosis, and adipocyte hypertrophy (Figures 5D–5F), followed by marked neutrophilia, compared with HFD-fed control mice (Figure 5G). By contrast, _Sema6d_[ΔCx3cr1] mice were vulnerable to HFD-induced obesity (Figure S4F). These results indicate that SEMA6D in neurons but not in MG plays a key role in regulating anxiogenic and autonomic responses.

Considering that the Tau-Cre mouse line exhibits Cre recombinase activity in neurons from most of the central nervous system,[39] we next deleted _Sema6d_ in particular brain regions, including the hypothalamus and cortex, by breeding LepR-Cre mice with _Sema6d_[fl/fl] mice (_Sema6d_[ΔLepR])[40] (Figure S4G). _Sema6d_[ΔLepR] mice exhibited unaltered anxiety-like behaviors and HFD-induced obesity compared with control mice (Figures S4H and S4I), indicating that hypothalamic and cortical SEMA6D are irrelevant to anxiogenic and autonomic responses.

SEMA6D maintains neural connectivity in the amygdala
To examine the global effects of _Sema6d_ deficiency in the brain, we next performed spatial transcriptomics on brain sections from WT and _Sema6d_[−/−] mice using Visium from 10× Genomics. We detected 61,863 ± 27,813 (WT) and 19,347 ± 10,575

(_Sema6d_[−/−]) unique molecular identifiers (UMIs), and 9,206 ± 984 (WT) and 5,987 ± 1,415 (_Sema6d_[−/−]) unique genes per spot (Figure S5A). The 8,381 transcriptomic profiles (WT 3,981 spots versus _Sema6d_[−/−] 4,400 spots) clustered according to brain regions using uniform manifold approximation and projection (UMAP) (Figures 6A and 6B). The spots of WT and _Sema6d_[−/−] mice largely overlapped, indicating that loss of SEMA6D did not perturb gross structural and transcriptional profiles of the brain (Figures 6B, S5B, and S5C).

To directly identify brain regions that function as interoceptive sites to coordinate anxiogenic and autonomic responses via SEMA6D, we queried _Sema6d_ and _Plxna4_ expression in the brain using our Visium dataset. Although _Sema6d_ was expressed widely in the brain, _Plxna4_ expression was restricted to specific regions, such as the amygdala and hippocampus (Figure 6C). We also validated the expression of _Sema6d_ and _Plxna4_ using _in situ_ hybridization methods. RNAscope revealed that _Sema6d_ was highly expressed in the inhibitory neurons (INs) of the central amygdala (CeA), whereas _Plxna4_ was selectively expressed in the basolateral amygdala (BLA), showing a complementary expression profile (Figure 6D). Given that CeA regulates autonomic and behavioral functions related to fear, pain, and stress,[23,41,42] we chose to focus on the amygdala.

To gain insights into the molecular pathways downstream of SEMA6D in the amygdala, we performed single-nucleus RNA-seq (snRNA-seq) on nuclei isolated from the amygdala of WT and _Sema6d_[−/−] mice using the 10× Genomics platform. After quality control filtering, we retained 17,656 nuclei (WT 10,143 nuclei versus _Sema6d_[−/−] 7,509 nuclei). On unsupervised clustering, the nuclei were separated into 25 cell types: INs (10,123 nuclei; IN1–9), excitatory neurons (2,991 nuclei; EN1–8), cholinergic neurons (132 nuclei; CN), MG (352 nuclei), astrocytes (1,581 nuclei; ASCs), oligodendrocytes (1,798 nuclei; ODC1–2), oligodendrocyte progenitor cells (370 nuclei; OPC), and endothelial cells (309 nuclei; END1–2), as classified by the gene expression of cell-type markers (Figures 6E and S6A). Each of the 25 clusters was detected in the WT and _Sema6d_[−/−] samples (Figures S6B and S6C). To spatially define these clusters, we integrated our Visium and snRNA-seq datasets. _Slc17a7_ and _Rspo2_ are highly expressed in the BLA, while _Gad2_ and _Tac2_ show region-specific expression in the CeA.[43–45] Based on the expression of these marker genes, we assigned the Visium spots to the BLA and CeA (Figure S6D). By creating modules for the BLA and CeA from our Visium experiments, we approximated the location of each snRNA-seq cell cluster in the BLA and CeA. This approach revealed that EN and IN clusters resided

---

Figure 4. SEMA6D expressed in non-hematopoietic cells regulates systemic metabolism and myelopoiesis

Bone marrow chimera mice were fed HFD for 12 weeks.

(A) Body weights. $n = 6$.

(B) Liver, eWAT, iWAT, and BAT weights. $n = 6–7$.

(C) Representative H&E-stained images of the liver, eWAT, iWAT, and BAT. Scale bars, 200 μm.

(D) Representative gross morphology of the liver, eWAT, iWAT, and BAT. Scale bars, 1 cm.

(E) eWAT and iWAT adipocyte sizes (area per adipocyte, μm²). $n = 6–7$.

(F) Representative FACS plots of MyP subpopulations in the BM.

(G) Proportions of CMPs, GMPs, and MEPs (versus MyPs) in the BM. $n = 4–6$.

(H) Representative FACS plots identifying neutrophils in the peripheral blood.

(I) Proportions of neutrophils in the peripheral blood. $n = 4–6$.

All data are presented as mean ± SEM. *$p < 0.05$, **$p < 0.01$, ***$p < 0.001$, ****$p < 0.0001$. n.s., not significant. Two-way ANOVA (A); one-way ANOVA (B, E, G, and I).
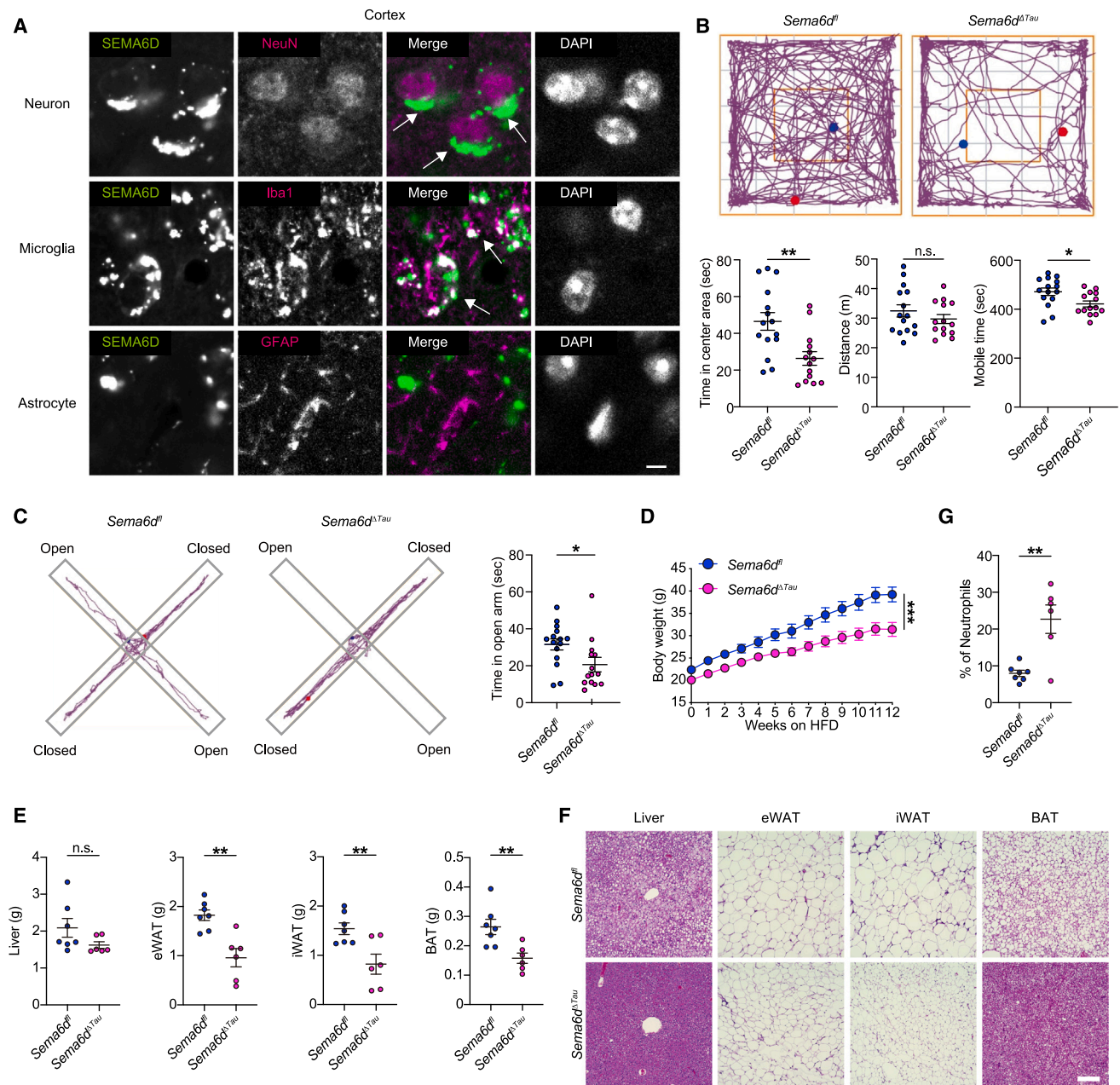
Figure 5. Neuron-derived SEMA6D plays an essential role in anxiogenic and autonomic responses

(A) A representative cortex image from a *Sema6d^{IRES-Cre/+}*;Ai6 mouse. White arrows indicate positive staining for SEMA6D⁺ neurons and microglia. Scale bars, 5 μm.

(B) Representative tracks, time spent in the center, travel distance, and mobile time of *Sema6d^{fl}* and *Sema6d^{ΔTau}* mice in OFT. n = 14–15.

(C) Representative tracks and time spent in the open arm of *Sema6d^{fl}* and *Sema6d^{ΔTau}* mice in the EPM test. n = 14–15.

(D–G) *Sema6d^{fl}* and *Sema6d^{ΔTau}* mice were fed an HFD for 12 weeks.

(D) Body weights. n = 6–7.

(E) Liver, eWAT, iWAT, and BAT weights. n = 6–7.

(F) Representative H&E-stained images of the liver, eWAT, iWAT, and BAT. Scale bars, 200 μm.

(G) Proportions of neutrophils in the peripheral blood. n = 6–7.

All data are presented as mean ± SEM. *p < 0.05, **p < 0.01, ***p < 0.001. n.s., not significant. Unpaired two-tailed Student's t test (B, C, E, and G); two-way ANOVA (D).

See also Figures S3 and S4.
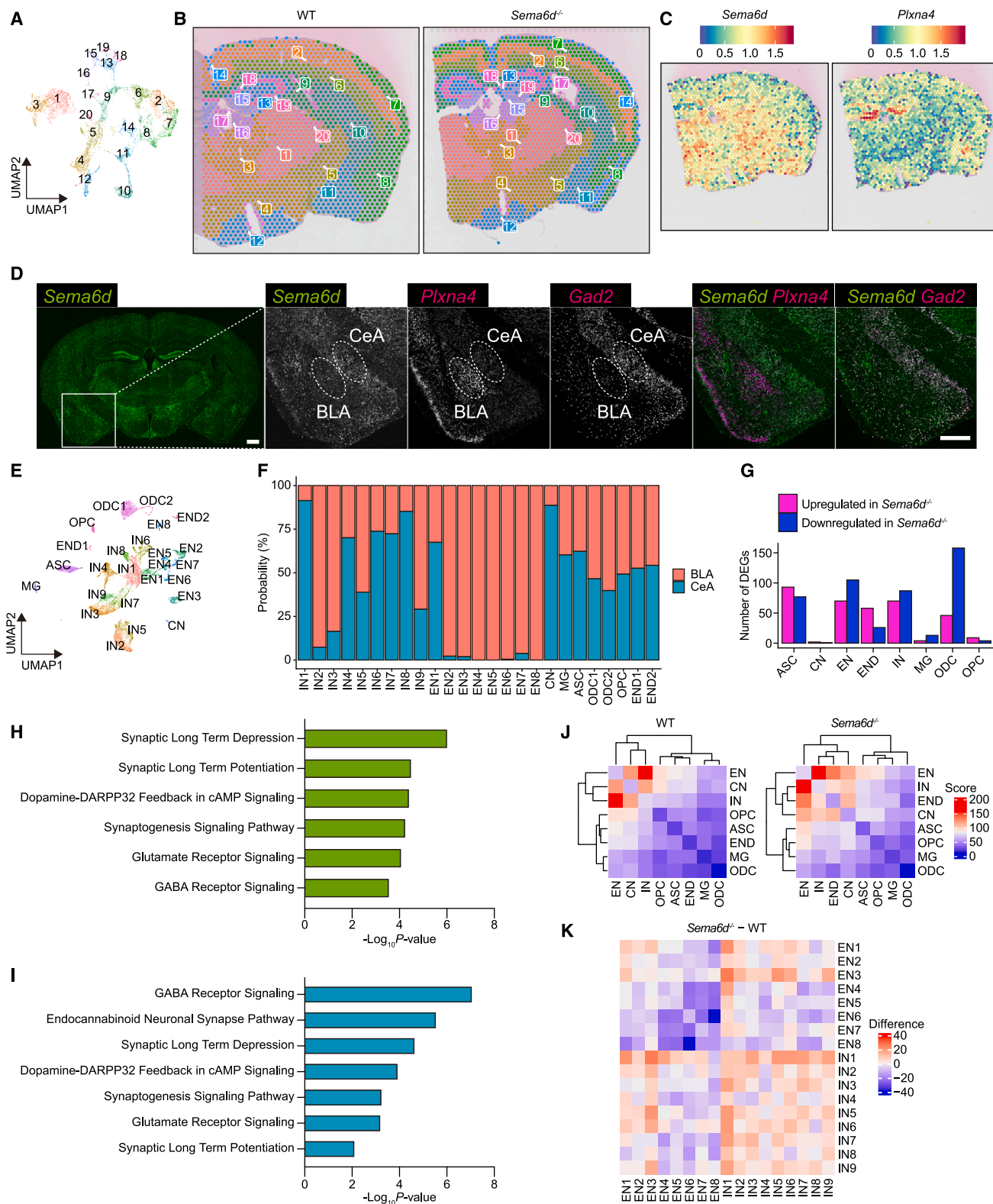
Figure 6. SEMA6D constructs neural circuits in the amygdala

(A–C) The brains of WT and *Sema6d*$^{-/-}$ mice were analyzed using Visium.

(A) UMAP visualization of the four brain sections, where dots correspond to an individual spot of a Visium Spatial Gene Expression Slide capture area.

(legend continued on next page)

mainly in the BLA and CeA, respectively, while MG, ASC, ODC, OPC, and END clusters were distributed equally between the BLA and CeA (Figure 6F).

To understand how individual clusters respond to *Sema6d* deficiency, we next identified the DEGs of each cell type. *Sema6d* deletion affected the transcriptomic profiles of IN, EN, ODC, ASC, and END clusters (Figure 6G). *Sema6d* and *Plxna4* were primarily expressed in the IN and EN clusters, respectively, whereas the ODC, ASC, and END clusters exhibited lower levels of *Sema6d* or *Plxna4* expression (Figure S6E). This complementary expression pattern of *Sema6d* and *Plxna4* suggests that SEMA6D-PLXNA4 signaling mediates the crosstalk between inhibitory and ENs. CeA neurons project to the sympathetic premotor neurons in the rostral ventrolateral medulla (RVLM), which in turn project to sympathetic preganglionic neurons and tightly regulate sympathetic outflow from the brain.[46–48] M-current through Kv7 channel in CeA-RVLM projecting neurons suppresses excessive sympathetic outflow.[49] We found that loss of *Sema6d* markedly suppressed the expression of *Kcnq3*, which encodes Kv7.3, in the EN and IN clusters (Figure S6F), suggesting that altered CeA-RVLM neural transmission causes enhanced sympathetic outflow in *Sema6d*$^{-/-}$ mice. Furthermore, DEGs in the EN and IN clusters were enriched in synaptic responses, such as synaptic LT potentiation/depression, synaptogenesis, glutamate receptor signaling, and GABA receptor signaling (Figures 6H and 6I). These results suggest that SEMA6D maintains neural connectivity in the amygdala.

We next examined the effect of *Sema6d* deficiency on neural connectivity in the amygdala by analyzing ligand-receptor interactions using CellPhoneDB.[50] In WT and *Sema6d*$^{-/-}$ samples, the interaction between EN and IN clusters was predominant (Figure 6J). Loss of *Sema6d* decreased the overall interactions of EN populations with IN populations (Figure 6K). To directly examine whether *Sema6d* deficiency affects neural projections from the BLA to the CeA, we injected a retrograde tracer, cholera toxin subunit B (CTB), into the CeA. We found no difference between WT and *Sema6d*$^{-/-}$ mice in the labeling of BLA neurons (Figure S6G). These results suggest that SEMA6D is important not for neural projections but for proper signal transduction in the amygdala.

SEMA6D regulates synaptic maturation and GABAergic transmission in the amygdala

We further examined the roles of SEMA6D in synaptic responses. We performed Golgi staining on WT and *Sema6d*$^{-/-}$

BLA pyramidal neurons to assess the spine morphology. Golgi staining revealed an increase in synaptic density driven by the retention of immature long thin spines in *Sema6d*$^{-/-}$ BLA pyramidal neurons (Figures 7A and 7B). Consistent with the altered spine morphology in *Sema6d*$^{-/-}$ BLA pyramidal neurons, *Sema6d* deficiency resulted in the decreased expression of postsynaptic markers, such as *Dlg4* and *Camk2a*, in EN clusters (Figure 7C). On the other hand, loss of SEMA6D did not affect the dendritic branching of BLA pyramidal neurons (Figures S7A and S7B). We also examined whether loss of *Sema6d* impairs signal transduction by neurotransmitters. Given the essential role of GABA in regulating anxiety and sympathetic activity,[51] we quantified the levels of GABA in WT and *Sema6d*$^{-/-}$ brains. Imaging mass spectrometry revealed that *Sema6d* deficiency decreased GABA levels in several brain regions, especially CeA (Figures 7D–7F). By contrast, loss of SEMA6D did not affect glutamate levels in each brain region, including BLA (Figures S7C–S7E). *Sema6d* deletion did not alter the expression of *Gad1* and *Gad2*, which encode the GABA synthetic enzymes, in IN clusters (Figure 7G). On the other hand, *Sema6d* deficiency upregulated the expression of *Slc6a1*, which encodes the GABA transporter, in ASC, CN, IN, and ODC clusters (Figure 7G). To determine whether defective GABAergic transmission is related to elevated anxiety in *Sema6d*$^{-/-}$ mice, we administered diazepam, a positive allosteric modulator of the GABA$_A$ receptor, to *Sema6d*$^{-/-}$ mice. The treatment reduced anxiety levels in these mice (Figure 7H). To directly determine whether amygdalar SEMA6D is involved in the regulation of anxiety and systemic metabolism, we stereotaxically injected AAV8-hSyn-GFP or AAV8-hSyn-Cre-GFP into the CeA of *Sema6d*$^{fl/fl}$ mice. CeA-specific loss of SEMA6D reduced the exploration time in the OF test and mitigated HFD-induced obesity, indicating that amygdalar SEMA6D is responsible for regulating anxiety and systemic metabolism (Figures 7I–7K and S7F). Thus, these results implicate amygdalar SEMA6D signaling in acquiring mature synaptic functions via spine formation and GABAergic transmission.

DISCUSSION

Our data demonstrate that amygdalar SEMA6D regulates neural, metabolic, and inflammatory outputs by maintaining synaptic responses, thereby presenting a critical association between brain function and peripheral neural-metabolic-immune interactions. Although previous studies focused on the peripheral crosstalk among the neural, metabolic, and immune systems and

---

(B) Spatial location of each cluster in Visium data.

(C) Spatial expression of *Sema6d* and *Plxna4* in WT brain.

(D) Representative images of RNAscope with *Sema6d*, *Plxna4*, and *Gad2* probes in the amygdala of WT mice. CeA, the central amygdala; BLA, the basolateral amygdala; Scale bars, 500 μm.

(E–K) The amygdalae of WT and *Sema6d*$^{-/-}$ mice were analyzed using snRNA-seq.

(E) UMAP visualization: dots correspond to individual nuclei for 17,656 nuclei profiled using snRNA-seq. INs, inhibitory neurons; ENs, excitatory neurons; CNs, cholinergic neurons; MG, microglia; ASCs, astrocytes; ODCs, oligodendrocytes; OPCs, oligodendrocyte progenitor cells; ENDs, endothelial cells.

(F) Spatial distribution of cell types defined by snRNA-seq mapped on a Visium slide.

(G) The number of DEGs for all cell clusters in the comparison between *Sema6d*$^{-/-}$ and WT mice.

(H and I) Top canonical pathways enriched by DEGs from *Sema6d*$^{-/-}$ EN (H) and IN (I).

(J and K) Heatmap showing the number of potential ligand-receptor pairs among the predicted cell types in each genotype (J) and the difference between WT and *Sema6d*$^{-/-}$ brains (K).

See also Figures S5 and S6.
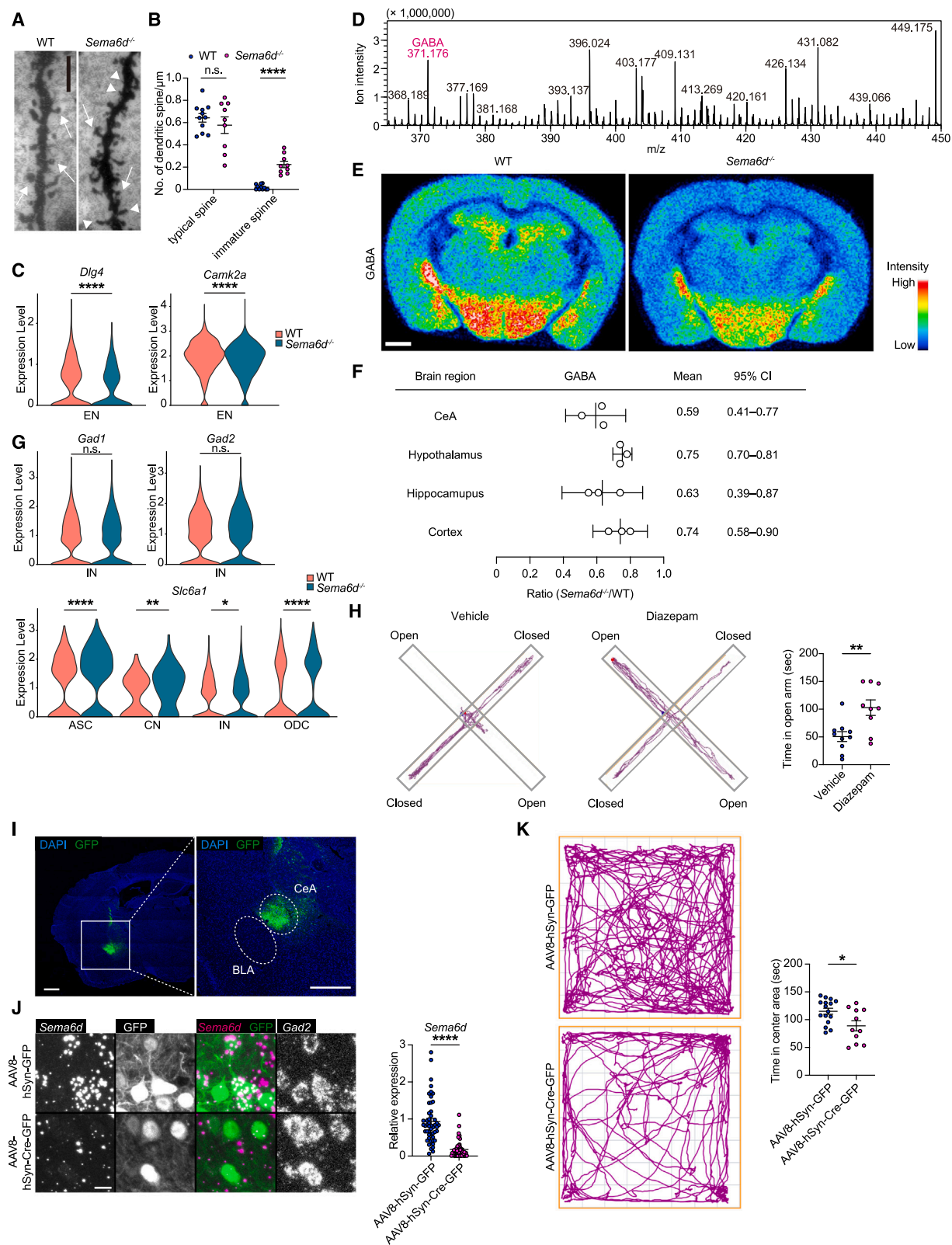
established the concepts of "neuroinflammation" and "immuno-metabolism," how the body detects and modulates the balance of this crosstalk has not yet been clarified.

Given that the central nervous system, including the brain, integrates external stimuli and coordinates the activity of the whole body, the question arises as to whether and how the brain regulates peripheral neural-metabolic-immune interactions. We focused here on the amygdala function, a critical brain region that regulates autonomic and behavioral responses related to fear, pain, and stress. When activated by emotional stimuli, such as fear and stress, the amygdala sends action potentials to efferent neurons that project to the brainstem and instigate a sympathetic response, promoting myelopoiesis in the BM and the development of atherosclerosis. Heightened amygdala activity due to psychosocial stress is related to cardiovascular disease events that are mediated by increased BM activity and arterial inflammation in humans.[52,53] However, the molecular machinery that regulates sympathetic outflow from the amygdala remains largely unknown. Our data suggest that SEMA6D-PLXNA4 signaling units between the CeA INs and BLA ENs are essential for maintaining the integrity of amygdalar neural circuits related to sympathetic responses. Notably, we found that SEMA6D regulated sympathetic outflow by maintaining GABAergic transmission. This finding is consistent with a previous report that impaired GABAergic transmission in the amygdala due to the loss of BDNF causes increased anxiety and sympathetic activity.[51] Since BDNF and semaphorin 7A share a common signaling pathway for synapse elimination in the cerebellum,[54] there may be a functional crosstalk between BDNF and SEMA6D in the amygdala. Although our transcriptomic data revealed that Sema6d deficiency upregulated the expression of GABA transporter in several types of cells, further studies are required to determine the mechanism for GABA reduction by Sema6d deficiency. Our data showed that systemic administration of diazepam mitigated anxiety in Sema6d⁻/⁻ mice. Given that SEMA6D is widely expressed in the brain, this experiment does not rule out the possibility that the effects of diazepam are carried out in brain regions other than the amygdala. However, our CeA-specific Sema6d deletion experiments

strongly indicate that the amygdala is the principal brain region that regulates anxiety via SEMA6D-mediated GABAergic signaling. Given that diazepam stimulates feeding,[55] it is difficult to assess the effects of diazepam on HFD-induced obesity independently from appetite regulation. Further studies are required to determine the effects of LT restoration of GABAergic signaling on metabolic defects in Sema6d⁻/⁻ mice.

Our findings also have clinical implications for pathologies of psychiatric diseases with metabolic and inflammatory complications. Although both weight gain and loss are associated with mental disorders, such as anxiety and depression,[56–59] the detailed molecular mechanism of this relationship has not been fully characterized. Previous GWASs revealed the genetic contribution of SEMA6D mutations to psychiatric diseases and traits, such as schizophrenia, attention-deficit hyperactivity disorder, and neuroticism.[18–20] However, other roles of SEMA6D in the brain have not been reported, except for regulating the contralateral projections of retinal axons.[11] Here, we demonstrated that the loss of Sema6d causes impaired synaptic maturation and GABAergic transmission in the amygdala, resembling the pathology of schizophrenia. The ratio of excitatory to inhibitory synapses is fairly constant across different brain regions, showing the maintenance of excitatory/inhibitory synaptic balance in the generation and maturation of functional neural circuits.[60,61] However, this synaptic homeostasis is perturbed in pathological conditions.[62,63] Schizophrenia is attributed to synaptic dysfunction, including altered synaptic formation and plasticity. Reduced spine density and increased immature spines were observed in patients with schizophrenia.[62] In addition, an imbalance between glutamatergic and GABAergic signaling was reported in patients with schizophrenia.[63] Considering the increased number of immature spines and decreased levels of GABA in Sema6d⁻/⁻ mice, SEMA6D is a potential therapeutic target for schizophrenia. Autonomic and immune abnormalities were also implicated in schizophrenia,[64–67] yet it remains unknown whether an upstream regulator of these abnormalities exists. Our findings revealed that the loss of Sema6d is sufficient to cause autonomic and immune dysfunctions, implying the importance of SEMA6D signaling in the pathogenesis of schizophrenia.

Figure 7. SEMA6D regulates synaptic maturation and GABAergic transmission

(A and B) WT and Sema6d⁻/⁻ mice were assessed for neuronal synapses in the BLA pyramidal neurons.

(A) Representative dendritic segments. Arrows and arrowheads indicate mature and immature spines, respectively. Scale bars, 5 μm.

(B) Spine density. n = 9–11.

(C) Violin plots of postsynaptic markers for the EN cluster.

(D–F) Imaging mass spectrometry of GABA in WT and Sema6d⁻/⁻ mice brains.

(D) Obtained product ion spectra.

(E) Representative images of GABA distribution in the brains. Scale bars, 1 mm.

(F) GABA levels in the brain regions. n = 3; mean and 95% confidence interval (95% CI).

(G) Violin plots showing the expression of Gad1, Gad2, and Slc6a1 in each cell cluster.

(H) Sema6d⁻/⁻ mice were intraperitoneally administered the vehicle or diazepam 30 min before the EPM test. Representative tracks and time spent in the open arm in the EPM test. n = 9–10.

(I–K) Sema6d^fl/fl mice were bilaterally injected with AAV8-hSyn-GFP or AAV8-hSyn-Cre-GFP into the CeA.

(I) A representative image showing AAV8-hSyn-GFP infection in the CeA. Scale bars, 500 μm.

(J) Representative images of RNAscope with Sema6d (magenta) and Gad2 (white) probes and GFP (green) in the CeA of AAV-injected Sema6d^fl/fl mice. Mean pixel intensities per CeA Gad2⁺ neurons of AAV-injected Sema6d^fl/fl mice are plotted for Sema6d. Scale bars, 10 μm. n = 50.

(K) Representative tracks and time spent in the center in OFT. n = 11–16.

Data are presented as mean ± SEM except for (F). *p < 0.05, **p < 0.01, ****p < 0.0001. n.s., not significant. Unpaired two-tailed Student's t tests (B, C, G, H, J, and K).

See also Figure S7.

Rare variants of *PLXNA4* are associated with human obesity.[68] These mutations reduced cell-surface expression of PLXNA4 *in vitro*, suggesting that reduced PLXNA4 signaling is associated with childhood obesity. By contrast, our data showed that complete deletion of PLXNA4 caused resistance to HFD-induced obesity. This contradiction could be due to several factors. The found rare variants were not statistically significant at the single gene level, indicating that we cannot estimate the burden of these variants in obesity with the current sample size. In addition, type-A PLXNs exhibit dual activities depending on the presence of neuropilin expression.[69]

Our results suggest that biphasic SEMA6D signaling coordinates the spatiotemporal regulation of inflammation. We previously revealed that mTOR-mediated induction of immune SEMA6D is essential for anti-inflammatory polarization of macrophages, leading to the suppression of local inflammation.[17] Here, we showed that neural SEMA6D regulates systemic hematopoietic responses under metabolic stress by tuning sympathetic signaling. Thus, SEMA6D orchestrates the immune system in a dual manner: (1) by promoting anti-inflammatory macrophage production in an immune cell-intrinsic manner to suppress local and acute inflammatory responses and (2) by modulating sympathetic outflow in an immune cell-extrinsic manner to suppress systemic and chronic inflammatory responses. Loss of *Sema6d* resulted in suppressed recruitment of inflammatory ATMs, indicating that immune SEMA6D signaling is not involved in coupling systemic metabolism and myelopoiesis. This phenomenon suggests that immune and neural SEMA6D signaling pathways are independently regulated in the HFD-induced obesity model. Given that a wide range of cells expresses SEMA6D, these two types of signaling may collaboratively maintain inflammatory responses in other conditions. Further studies are required to reveal the overlap of the two SEMA6D signaling modes.

In conclusion, our study illustrates a previously unknown mechanism of brain-mediated coupling of the neural, metabolic, and inflammatory responses. Defective SEMA6D signaling leads to perturbed neural activity in the amygdala, followed by abnormal emotional, metabolic, and hematopoietic responses. Thus, this study adds another perspective to the understanding of neural-metabolic-immune interactions and, presumably, an avenue for therapeutic intervention in psychiatric, metabolic, and inflammatory diseases through augmenting SEMA6D signaling by microinjection of its mRNA or recombinant proteins.

STAR★METHODS

Detailed methods are provided in the online version of this paper and include the following:

SUPPLEMENTAL INFORMATION

Supplemental information can be found online at https://doi.org/10.1016/j.neuron.2024.06.017.

ACKNOWLEDGMENTS

AUTHOR CONTRIBUTIONS

Conceptualization: Y. Nakanishi, M. Izumi, S. Kang, and A.K.; funding acquisition: Y. Nakanishi, S. Kang, and A.K.; investigation: Y. Nakanishi, M. Izumi, H.M., D.D., M. Naito, Y.M., Y.Y., T.M., Y. Noda, K.N., and S. Kang; methodology: Y. Nakanishi, M. Izumi, H.M., Y.K., D.D., H.T., S. Koyama, M. Nishide, S.N., F.S., D.O., M. Ikawa, S.S., S. Kang, and A.K.; project administration: S. Kang and A.K.; supervision: S. Kang and A.K.; visualization: Y. Nakanishi, M. Izumi, and D.D.; writing – original draft: Y. Nakanishi, M. Izumi, S. Kang, and A.K. writing – review and editing: all authors.

REFERENCES

1. Wolf, Y., Boura-Halfon, S., Cortese, N., Haimon, Z., Sar Shalom, H.S., Kuperman, Y., Kalchenko, V., Brandis, A., David, E., Segal-Hayoun, Y., et al. (2017). Brown-adipose-tissue macrophages control tissue innervation and homeostatic energy expenditure. Nat. Immunol. *18*, 665–674. https://doi.org/10.1038/ni.3746.

2. Hu, B., Jin, C., Zeng, X., Resch, J.M., Jedrychowski, M.P., Yang, Z., Desai, B.N., Banks, A.S., Lowell, B.B., Mathis, D., and Spiegelman, B.M. (2020). γδT cells and adipocyte IL-17RC control fat innervation and thermogenesis. Nature *578*, 610–614. https://doi.org/10.1038/s41586-020-2028-z.

3. Adori, C., Daraio, T., Kuiper, R., Barde, S., Horvathova, L., Yoshitake, T., Ihnatko, R., Valladolid-Acebes, I., Vercruysse, P., Wellendorf, A.M., et al. (2021). Disorganization and degeneration of liver sympathetic innervations in nonalcoholic fatty liver disease revealed by 3D imaging. Sci. Adv. *7*, eabg5733. https://doi.org/10.1126/sciadv.abg5733.

4. Liu, K., Yang, L., Wang, G., Liu, J., Zhao, X., Wang, Y., Li, J., and Yang, J. (2021). Metabolic stress drives sympathetic neuropathy within the liver. Cell Metab. *33*, 666–675.e4. https://doi.org/10.1016/j.cmet.2021.01.012.

5. Locke, A.E., Kahali, B., Berndt, S.I., Justice, A.E., Pers, T.H., Day, F.R., Powell, C., Vedantam, S., Buchkovich, M.L., Yang, J., et al. (2015). Genetic studies of body mass index yield new insights for obesity biology. Nature *518*, 197–206. https://doi.org/10.1038/nature14177.

6. Koren, T., Yifa, R., Amer, M., Krot, M., Boshnak, N., Ben-Shaanan, T.L., Azulay-Debby, H., Zalayat, I., Avishai, E., Hajjo, H., et al. (2021). Insular cortex neurons encode and retrieve specific immune responses. Cell *184*, 5902–5915.e17. https://doi.org/10.1016/j.cell.2021.10.013.

7. Teratani, T., Mikami, Y., Nakamoto, N., Suzuki, T., Harada, Y., Okabayashi, K., Hagihara, Y., Taniki, N., Kohno, K., Shibata, S., et al. (2020). The liver-brain-gut neural arc maintains the Treg cell niche in the gut. Nature *585*, 591–596. https://doi.org/10.1038/s41586-020-2425-3.

8. Weiner, J.A., Jontes, J.D., and Burgess, R.W. (2013). Introduction to mechanisms of neural circuit formation. Front. Mol. Neurosci. *6*, 12. https://doi.org/10.3389/fnmol.2013.00012.

9. Pasterkamp, R.J. (2012). Getting neural circuits into shape with semaphorins. Nat. Rev. Neurosci. *13*, 605–618. https://doi.org/10.1038/nrn3302.

10. Yoshida, Y. (2012). Semaphorin signaling in vertebrate neural circuit assembly. Front. Mol. Neurosci. *5*, 71. https://doi.org/10.3389/fnmol.2012.00071.

11. Kuwajima, T., Yoshida, Y., Takegahara, N., Petros, T.J., Kumanogoh, A., Jessell, T.M., Sakurai, T., and Mason, C. (2012). Optic chiasm presentation of semaphorin6D in the context of plexin-A1 and Nr-CAM promotes retinal axon midline crossing. Neuron *74*, 676–690. https://doi.org/10.1016/j.neuron.2012.03.025.

12. Gu, Z., Kalambogias, J., Yoshioka, S., Han, W., Li, Z., Kawasawa, Y.I., Pochareddy, S., Li, Z., Liu, F., Xu, X., et al. (2017). Control of species-dependent cortico-motoneuronal connections underlying manual dexterity. Science *357*, 400–404. https://doi.org/10.1126/science.aan3721.

13. Toyofuku, T., Zhang, H., Kumanogoh, A., Takegahara, N., Suto, F., Kamei, J., Aoki, K., Yabuki, M., Hori, M., Fujisawa, H., and Kikutani, H. (2004a). Dual roles of Sema6D in cardiac morphogenesis through region-specific association of its receptor, Plexin-A1, with off-track and vascular endothelial growth factor receptor type 2. Genes Dev. *18*, 435–447. https://doi.org/10.1101/gad.1167304.

14. Toyofuku, T., Zhang, H., Kumanogoh, A., Takegahara, N., Yabuki, M., Harada, K., Hori, M., and Kikutani, H. (2004b). Guidance of myocardial patterning in cardiac development by Sema6D reverse signalling. Nat. Cell Biol. *6*, 1204–1211. https://doi.org/10.1038/ncb1193.

15. Takegahara, N., Takamatsu, H., Toyofuku, T., Tsujimura, T., Okuno, T., Yukawa, K., Mizui, M., Yamamoto, M., Prasad, D.V.R., Suzuki, K., et al. (2006). Plexin-A1 and its interaction with DAP12 in immune responses and bone homeostasis. Nat. Cell Biol. *8*, 615–622. https://doi.org/10.1038/ncb1416.

16. O'Connor, B.P., Eun, S.Y., Ye, Z., Zozulya, A.L., Lich, J.D., Moore, C.B., Iocca, H.A., Roney, K.E., Holl, E.K., Wu, Q.P., et al. (2008). Semaphorin 6D regulates the late phase of CD4+ T cell primary immune responses. Proc. Natl. Acad. Sci. USA *105*, 13015–13020. https://doi.org/10.1073/pnas.0803386105.

17. Kang, S., Nakanishi, Y., Kioi, Y., Okuzaki, D., Kimura, T., Takamatsu, H., Koyama, S., Nojima, S., Nishide, M., Hayama, Y., et al. (2018). Semaphorin 6D reverse signaling controls macrophage lipid metabolism and anti-inflammatory polarization. Nat. Immunol. *19*, 561–570. https://doi.org/10.1038/s41590-018-0108-0.

18. Luciano, M., Hagenaars, S.P., Davies, G., Hill, W.D., Clarke, T.K., Shirali, M., Harris, S.E., Marioni, R.E., Liewald, D.C., Fawns-Ritchie, C., et al. (2018). Association analysis in over 329,000 individuals identifies 116 independent variants influencing neuroticism. Nat. Genet. *50*, 6–11. https://doi.org/10.1038/s41588-017-0013-8.

19. Wang, Z., Li, P., Wu, T., Zhu, S., Deng, L., and Cui, G. (2018). Axon guidance pathway genes are associated with schizophrenia risk. Exp. Ther. Med. *16*, 4519–4526. https://doi.org/10.3892/etm.2018.6781.

20. Demontis, D., Walters, R.K., Martin, J., Mattheisen, M., Als, T.D., Agerbo, E., Baldursson, G., Belliveau, R., Bybjerg-Grauholm, J., Bækvad-Hansen, M., et al. (2019). Discovery of the first genome-wide significant risk loci for attention deficit/hyperactivity disorder. Nat. Genet. *51*, 63–75. https://doi.org/10.1038/s41588-018-0269-7.

21. Bulik-Sullivan, B.K., Loh, P.R., Finucane, H.K., Ripke, S., Yang, J., Schizophrenia Working Group of the Psychiatric; Genomics Consortium, Patterson, N., Daly, M.J., Price, A.L., and Neale, B.M. (2015). LD Score regression distinguishes confounding from polygenicity in genome-wide association studies. Nat. Genet. *47*, 291–295. https://doi.org/10.1038/ng.3211.

22. Watanabe, K., Stringer, S., Frei, O., Umićević Mirkov, M., de Leeuw, C., Polderman, T.J.C., van der Sluis, S., Andreassen, O.A., Neale, B.M., and Posthuma, D. (2019). A global overview of pleiotropy and genetic architecture in complex traits. Nat. Genet. *51*, 1339–1348. https://doi.org/10.1038/s41588-019-0481-0.

23. Calhoon, G.G., and Tye, K.M. (2015). Resolving the neural circuits of anxiety. Nat. Neurosci. *18*, 1394–1404. https://doi.org/10.1038/nn.4101.

24. Simon, P., Dupuis, R., and Costentin, J. (1994). Thigmotaxis as an index of anxiety in mice. Influence of dopaminergic transmissions. Behav. Brain Res. *61*, 59–64. https://doi.org/10.1016/0166-4328(94)90008-6.

25. Walf, A.A., and Frye, C.A. (2007). The use of the elevated plus maze as an assay of anxiety-related behavior in rodents. Nat. Protoc. *2*, 322–328. https://doi.org/10.1038/nprot.2007.44.

26. Schmidt, M.I., Duncan, B.B., Sharrett, A.R., Lindberg, G., Savage, P.J., Offenbacher, S., Azambuja, M.I., Tracy, R.P., and Heiss, G. (1999). Markers of inflammation and prediction of diabetes mellitus in adults (atherosclerosis risk in communities study): a cohort study. Lancet *353*, 1649–1652. https://doi.org/10.1016/S0140-6736(99)01046-6.

27. Ford, E.S. (2002). Leukocyte count, erythrocyte sedimentation rate, and diabetes incidence in a national sample of US adults. Am. J. Epidemiol. *155*, 57–64. https://doi.org/10.1093/aje/155.1.57.

28. Kullo, I.J., Hensrud, D.D., and Allison, T.G. (2002). Comparison of numbers of circulating blood monocytes in men grouped by body mass index (<25, 25 to <30, > or =30). Am. J. Cardiol. *89*, 1441–1443. https://doi.org/10.1016/S0002-9149(02)02366-4.

29. Ohshita, K., Yamane, K., Hanafusa, M., Mori, H., Mito, K., Okubo, M., Hara, H., and Kohno, N. (2004). Elevated white blood cell count in subjects with impaired glucose tolerance. Diabetes Care *27*, 491–496. https://doi.org/10.2337/diacare.27.2.491.

30. Olefsky, J.M., and Glass, C.K. (2010). Macrophages, inflammation, and insulin resistance. Annu. Rev. Physiol. *72*, 219–246. https://doi.org/10.1146/annurev-physiol-021909-135846.

31. Ito, K., and Suda, T. (2014). Metabolic requirements for the maintenance of self-renewing stem cells. Nat. Rev. Mol. Cell Biol. *15*, 243–256. https://doi.org/10.1038/nrm3772.

32. Mootha, V.K., Lindgren, C.M., Eriksson, K.F., Subramanian, A., Sihag, S., Lehar, J., Puigserver, P., Carlsson, E., Ridderstråle, M., Laurila, E., et al. (2003). PGC-1alpha-responsive genes involved in oxidative phosphorylation are coordinately downregulated in human diabetes. Nat. Genet. *34*, 267–273. https://doi.org/10.1038/ng1180.

33. Subramanian, A., Tamayo, P., Mootha, V.K., Mukherjee, S., Ebert, B.L., Gillette, M.A., Paulovich, A., Pomeroy, S.L., Golub, T.R., Lander, E.S., and Mesirov, J.P. (2005). Gene set enrichment analysis: a knowledge-based approach for interpreting genome-wide expression profiles. Proc. Natl. Acad. Sci. USA *102*, 15545–15550. https://doi.org/10.1073/pnas.0506580102.

34. Heine, M., Fischer, A.W., Schlein, C., Jung, C., Straub, L.G., Gottschling, K., Mangels, N., Yuan, Y., Nilsson, S.K., Liebscher, G., et al. (2018). Lipolysis triggers a systemic insulin response essential for efficient energy replenishment of activated brown adipose tissue in mice. Cell Metab. *28*, 644–655.e4. https://doi.org/10.1016/j.cmet.2018.06.020.

35. Heidt, T., Sager, H.B., Courties, G., Dutta, P., Iwamoto, Y., Zaltsman, A., von Zur Muhlen, C., Bode, C., Fricchione, G.L., Denninger, J., et al. (2014). Chronic variable stress activates hematopoietic stem cells. Nat. Med. *20*, 754–758. https://doi.org/10.1038/nm.3589.

36. Kanehisa, M., Furumichi, M., Tanabe, M., Sato, Y., and Morishima, K. (2017). KEGG: new perspectives on genomes, pathways, diseases and drugs. Nucleic Acids Res. *45*, D353–D361. https://doi.org/10.1093/nar/gkw1092.

37. Madisen, L., Zwingman, T.A., Sunkin, S.M., Oh, S.W., Zariwala, H.A., Gu, H., Ng, L.L., Palmiter, R.D., Hawrylycz, M.J., Jones, A.R., et al. (2010). A robust and high-throughput Cre reporting and characterization system for the whole mouse brain. Nat. Neurosci. *13*, 133–140. https://doi.org/10.1038/nn.2467.

38. Weber, M.D., McKim, D.B., Niraula, A., Witcher, K.G., Yin, W., Sobol, C.G., Wang, Y., Sawicki, C.M., Sheridan, J.F., and Godbout, J.P. (2019). The influence of microglial elimination and repopulation on stress sensitization induced by repeated social defeat. Biol. Psychiatry *85*, 667–678. https://doi.org/10.1016/j.biopsych.2018.10.009.

39. Muramatsu, K., Hashimoto, Y., Uemura, T., Kunii, M., Harada, R., Sato, T., Morikawa, A., and Harada, A. (2008). Neuron-specific recombination by Cre recombinase inserted into the murine tau locus. Biochem. Biophys. Res. Commun. *370*, 419–423. https://doi.org/10.1016/j.bbrc.2008.03.103.

40. DeFalco, J., Tomishima, M., Liu, H., Zhao, C., Cai, X., Marth, J.D., Enquist, L., and Friedman, J.M. (2001). Virus-assisted mapping of neural inputs to a feeding center in the hypothalamus. Science *291*, 2608–2613. https://doi.org/10.1126/science.1056602.

41. Chapp, A.D., Gui, L., Huber, M.J., Liu, J., Larson, R.A., Zhu, J., Carter, J.R., and Chen, Q.H. (2014). Sympathoexcitation and pressor responses induced by ethanol in the central nucleus of amygdala involves activation of NMDA receptors in rats. Am. J. Physiol. Heart Circ. Physiol. *307*, H701–H709. https://doi.org/10.1152/ajpheart.00005.2014.

42. Pomrenze, M.B., Tovar-Diaz, J., Blasio, A., Maiya, R., Giovanetti, S.M., Lei, K., Morikawa, H., Hopf, F.W., and Messing, R.O. (2019). A corticotropin releasing factor network in the extended amygdala for anxiety. J. Neurosci. *39*, 1030–1043. https://doi.org/10.1523/JNEUROSCI.2143-18.2018.

43. Fremeau, R.T., Jr., Voglmaier, S., Seal, R.P., and Edwards, R.H. (2004). VGLUTs define subsets of excitatory neurons and suggest novel roles for glutamate. Trends Neurosci. *27*, 98–103. https://doi.org/10.1016/j.tins.2003.11.005.

44. Kim, J., Pignatelli, M., Xu, S., Itohara, S., and Tonegawa, S. (2016). Antagonistic negative and positive neurons of the basolateral amygdala. Nat. Neurosci. *19*, 1636–1646. https://doi.org/10.1038/nn.4414.

45. Kim, J., Zhang, X., Muralidhar, S., LeBlanc, S.A., and Tonegawa, S. (2017). Basolateral to central amygdala neural circuits for appetitive behaviors. Neuron *93*, 1464–1479.e5. https://doi.org/10.1016/j.neuron.2017.02.034.

46. Bowman, B.R., Kumar, N.N., Hassan, S.F., McMullan, S., and Goodchild, A.K. (2013). Brain sources of inhibitory input to the rat rostral ventrolateral medulla. J. Comp. Neurol. *521*, 213–232. https://doi.org/10.1002/cne.23175.

47. Gilbey, M.P., and Spyer, K.M. (1993). Essential organization of the sympathetic nervous system. Baillieres Clin. Endocrinol. Metab. *7*, 259–278. https://doi.org/10.1016/s0950-351x(05)80177-6.

48. Oshima, N., McMullan, S., Goodchild, A.K., and Pilowsky, P.M. (2006). A monosynaptic connection between baroinhibited neurons in the RVLM and IML in Sprague-Dawley rats. Brain Res. *1089*, 153–161. https://doi.org/10.1016/j.brainres.2006.03.024.

49. Sheng, Z.F., Zhang, H., Zheng, P., Chen, S., Gu, Z., Zhou, J.J., Phaup, J.G., Chang, H.M., Yeh, E.T.H., Pan, H.L., and Li, D.P. (2022). Impaired Kv7 channel activity in the central amygdala contributes to elevated sympathetic outflow in hypertension. Cardiovasc. Res. *118*, 585–596. https://doi.org/10.1093/cvr/cvab031.

50. Garcia-Alonso, L., Handfield, L.F., Roberts, K., Nikolakopoulou, K., Fernando, R.C., Gardner, L., Woodhams, B., Arutyunyan, A., Polanski, K., Hoo, R., et al. (2021). Mapping the temporal and spatial dynamics of the human endometrium in vivo and in vitro. Nat. Genet. *53*, 1698–1711. https://doi.org/10.1038/s41588-021-00972-2.

51. Xie, X., Yang, H., An, J.J., Houtz, J., Tan, J.W., Xu, H., Liao, G.Y., Xu, Z.X., and Xu, B. (2019). Activation of anxiogenic circuits instigates resistance to diet-induced obesity via increased energy expenditure. Cell Metab. *29*, 917–931.e4. https://doi.org/10.1016/j.cmet.2018.12.018.

52. Tawakol, A., Ishai, A., Takx, R.A., Figueroa, A.L., Ali, A., Kaiser, Y., Truong, Q.A., Solomon, C.J., Calcagno, C., Mani, V., et al. (2017). Relation between resting amygdalar activity and cardiovascular events: a longitudinal and cohort study. Lancet *389*, 834–845. https://doi.org/10.1016/S0140-6736(16)31714-7.

53. Powell-Wiley, T.M., Dey, A.K., Rivers, J.P., Chaturvedi, A., Andrews, M.R., Ceasar, J.N., Claudel, S.E., Mitchell, V.M., Ayers, C., Tamura, K., et al. (2021). Chronic stress-related neural activity associates with subclinical cardiovascular disease in a community-based cohort: data from the Washington, D.C. cardiovascular health and needs assessment. Front. Cardiovasc. Med. *8*, 599341. https://doi.org/10.3389/fcvm.2021.599341.

54. Choo, M., Miyazaki, T., Yamazaki, M., Kawamura, M., Nakazawa, T., Zhang, J., Tanimura, A., Uesaka, N., Watanabe, M., Sakimura, K., and Kano, M. (2017). Retrograde BDNF to TrkB signaling promotes synapse elimination in the developing cerebellum. Nat. Commun. *8*, 195. https://doi.org/10.1038/s41467-017-00260-w.

55. Berridge, K.C., and Peciña, S. (1995). Benzodiazepines, appetite, and taste palatability. Neurosci. Biobehav. Rev. *19*, 121–131. https://doi.org/10.1016/0149-7634(94)00026-w.

56. Anderson, S.E., Cohen, P., Naumova, E.N., and Must, A. (2006). Association of depression and anxiety disorders with weight change in a prospective community-based study of children followed up into adulthood. Arch. Pediatr. Adolesc. Med. *160*, 285–291. https://doi.org/10.1001/archpedi.160.3.285.

57. de Wit, L., Luppino, F., van Straten, A., Penninx, B., Zitman, F., and Cuijpers, P. (2010). Depression and obesity: a meta-analysis of community-based studies. Psychiatry Res. *178*, 230–235. https://doi.org/10.1016/j.psychres.2009.04.015.

58. Rofey, D.L., Kolko, R.P., Iosif, A.M., Silk, J.S., Bost, J.E., Feng, W., Szigethy, E.M., Noll, R.B., Ryan, N.D., and Dahl, R.E. (2009). A longitudinal study of childhood depression and anxiety in relation to weight gain. Child Psychiatry Hum. Dev. *40*, 517–526. https://doi.org/10.1007/s10578-009-0141-1.

59. McCrea, R.L., Berger, Y.G., and King, M.B. (2012). Body mass index and common mental disorders: exploring the shape of the association and its moderation by age, gender and education. Int. J. Obes. (Lond) *36*, 414–421. https://doi.org/10.1038/ijo.2011.65.

60. Hsu, A., Luebke, J.I., and Medalla, M. (2017). Comparative ultrastructural features of excitatory synapses in the visual and frontal cortices of the adult mouse and monkey. J. Comp. Neurol. *525*, 2175–2191. https://doi.org/10.1002/cne.24196.

61. Cline, H. (2005). Synaptogenesis: a balancing act between excitation and inhibition. Curr. Biol. *15*, R203–R205. https://doi.org/10.1016/j.cub.2005.03.010.

62. Penzes, P., Cahill, M.E., Jones, K.A., VanLeeuwen, J.E., and Woolfrey, K.M. (2011). Dendritic spine pathology in neuropsychiatric disorders. Nat. Neurosci. *14*, 285–293. https://doi.org/10.1038/nn.2741.

63. Marín, O. (2012). Interneuron dysfunction in psychiatric disorders. Nat. Rev. Neurosci. *13*, 107–120. https://doi.org/10.1038/nrn3155.

64. Bustan, Y., Drapisz, A., Ben Dor, D.H., Avrahami, M., Schwartz-Lifshitz, M., Weizman, A., and Barzilay, R. (2018). Elevated neutrophil to lympho-cyte ratio in non-affective psychotic adolescent inpatients: Evidence for early association between inflammation and psychosis. Psychiatry Res. *262*, 149–153. https://doi.org/10.1016/j.psychres.2018.02.002.

65. Brinn, A., and Stone, J. (2020). Neutrophil-lymphocyte ratio across psychi-atric diagnoses: a cross-sectional study using electronic health records. BMJ Open *10*, e036859. https://doi.org/10.1136/bmjopen-2020-036859.

66. Steiner, J., Frodl, T., Schiltz, K., Dobrowolny, H., Jacobs, R., Fernandes, B.S., Guest, P.C., Meyer-Lotz, G., Borucki, K., Bahn, S., et al. (2020). Innate immune cells and C-reactive protein in acute first-episode psycho-sis and schizophrenia: relationship to psychopathology and treatment. Schizophr. Bull. *46*, 363–373. https://doi.org/10.1093/schbul/sbz068.

67. Stogios, N., Gdanski, A., Gerretsen, P., Chintoh, A.F., Graff-Guerrero, A., Rajji, T.K., Remington, G., Hahn, M.K., and Agarwal, S.M. (2021). Autonomic nervous system dysfunction in schizophrenia: impact on cognitive and metabolic health. npj Schizophr. *7*, 22. https://doi.org/10.1038/s41537-021-00151-6.

68. van der Klaauw, A.A., Croizier, S., Mendes de Oliveira, E., Stadler, L.K.J., Park, S., Kong, Y., Banton, M.C., Tandon, P., Hendricks, A.E., Keogh, J.M., et al. (2019). Human semaphorin 3 variants link melanocortin circuit development and energy balance. Cell *176*, 729–742.e18. https://doi.org/10.1016/j.cell.2018.12.009.

69. Hayashi, M., Nakashima, T., Taniguchi, M., Kodama, T., Kumanogoh, A., and Takayanagi, H. (2012). Osteoprotection by semaphorin 3A. Nature *485*, 69–74. https://doi.org/10.1038/nature11000.

70. Suto, F., Ito, K., Uemura, M., Shimizu, M., Shinkawa, Y., Sanbo, M., Shinoda, T., Tsuboi, M., Takashima, S., Yagi, T., and Fujisawa, H. (2005). Plexin-a4 mediates axon-repulsive activities of both secreted and transmembrane semaphorins and plays roles in nerve fiber guidance. J. Neurosci. *25*, 3628–3637. https://doi.org/10.1523/JNEUROSCI.4480-04.2005.

71. Takamatsu, H., Takegahara, N., Nakagawa, Y., Tomura, M., Taniguchi, M., Friedel, R.H., Rayburn, H., Tessier-Lavigne, M., Yoshida, Y., Okuno, T., et al. (2010). Semaphorins guide the entry of dendritic cells into the lym-phatics by activating myosin II. Nat. Immunol. *11*, 594–600. https://doi.org/10.1038/ni.1885.

72. Okabe, K., Kobayashi, S., Yamada, T., Kurihara, T., Tai-Nagara, I., Miyamoto, T., Mukouyama, Y.S., Sato, T.N., Suda, T., Ema, M., and Kubota, Y. (2014). Neurons limit angiogenesis by titrating VEGF in retina. Cell *159*, 584–596. https://doi.org/10.1016/j.cell.2014.09.025.

73. Hao, Y., Hao, S., Andersen-Nissen, E., Mauck, W.M., 3rd, Zheng, S., Butler, A., Lee, M.J., Wilk, A.J., Darby, C., Zager, M., et al. (2021). Integrated analysis of multimodal single-cell data. Cell *184*, 3573–3587.e29. https://doi.org/10.1016/j.cell.2021.04.048.

74. Loza, M., Teraguchi, S., Standley, D.M., and Diez, D. (2022). Unbiased integration of single cell transcriptome replicates. NAR Genom. Bioinform. *4*, lqac022. https://doi.org/10.1093/nargab/lqac022.

75. Janowska-Wieczorek, A., Majka, M., Kijowski, J., Baj-Krzyworzeka, M., Reca, R., Turner, A.R., Ratajczak, J., Emerson, S.G., Kowalska, M.A., and Ratajczak, M.Z. (2001). Platelet-derived microparticles bind to he-matopoietic stem/progenitor cells and enhance their engraftment. Blood *98*, 3143–3149. https://doi.org/10.1182/blood.V98.10.3143.

76. Yona, S., Kim, K.W., Wolf, Y., Mildner, A., Varol, D., Breker, M., Strauss-Ayali, D., Viukov, S., Guilliams, M., Misharin, A., et al. (2013). Fate mapping reveals origins and dynamics of monocytes and tissue macrophages un-der homeostasis. Immunity *38*, 79–91. https://doi.org/10.1016/j.immuni.2012.12.001.

77. Logan, M., Martin, J.F., Nagy, A., Lobe, C., Olson, E.N., and Tabin, C.J. (2002). Expression of Cre Recombinase in the developing mouse limb bud driven by a Prxl enhancer. Genesis *33*, 77–80. https://doi.org/10.1002/gene.10092.

78. Noda, T., Sakurai, N., Nozawa, K., Kobayashi, S., Devlin, D.J., Matzuk, M.M., and Ikawa, M. (2019). Nine genes abundantly expressed in the epididymis are not essential for male fecundity in mice. Andrology *7*, 644–653. https://doi.org/10.1111/andr.12621.

79. Naito, Y., Hino, K., Bono, H., and Ui-Tei, K. (2015). CRISPRdirect: software for designing CRISPR/Cas guide RNA with reduced off-target sites. Bioinformatics *31*, 1120–1123. https://doi.org/10.1093/bioinformatics/btu743.

80. Chang, X., Liu, Y., Hahn, C-G., Gur, R.E., Sleiman, P.M.A., and Hakonarson, H. (2017). RNA-seq analysis of amygdala tissue reveals char-acteristic expression profiles in schizophrenia. Transl. Psychiatry *7*, e1203. https://doi.org/10.1038/tp.2017.154.

81. Okazaki, M., and Yamashita, S. (2016). Recent advances in analytical methods on lipoprotein subclasses: calculation of particle numbers from lipid levels by gel permeation HPLC using "spherical particle model". J. Oleo Sci. *65*, 265–282. https://doi.org/10.5650/jos.ess16020.

82. Galarraga, M., Campión, J., Muñoz-Barrutia, A., Boqué, N., Moreno, H., Martínez, J.A., Milagro, F., and Ortiz-de-Solórzano, C. (2012). Adiposoft: automated software for the analysis of white adipose tissue cellularity in histological sections. J. Lipid Res. *53*, 2791–2796. https://doi.org/10.1194/jlr.D023788.

83. Traag, V.A., Waltman, L., and van Eck, N.J. (2019). From Louvain to Leiden: guaranteeing well-connected communities. Sci. Rep. *9*, 5233. https://doi.org/10.1038/s41598-019-41695-z.

84. Arshadi, C., Günther, U., Eddison, M., Harrington, K.I.S., and Ferreira, T.A. (2021). SNT: a unifying toolbox for quantification of neuronal anatomy. Nat. Methods *18*, 374–377. https://doi.org/10.1038/s41592-021-01105-7.

85. Shariatgorji, M., Nilsson, A., Fridjonsdottir, E., Vallianatou, T., Källback, P., Katan, L., Sävmarker, J., Mantas, I., Zhang, X., Bezard, E., et al. (2019). Comprehensive mapping of neurotransmitter networks by MALDI-MS im-aging. Nat. Methods *16*, 1021–1028. https://doi.org/10.1038/s41592-019-0551-3.

STAR★METHODS

KEY RESOURCES TABLE

REAGENT or RESOURCE	SOURCE	IDENTIFIER
Antibodies		
Alexa 488 anti-rabbit	Invitrogen	Cat# A11070; RRID: AB_2534114
Alexa 647 anti-mouse	Invitrogen	Cat# A21237; RRID: AB_2535806
Alexa 647 anti-rabbit	Invitrogen	Cat# A21246; RRID: AB_2535814
Armenian hamster anti-mouse CD11c (clone HL3)	BD Pharmingen	Cat# 553801; RRID: AB_396683
Armenian hamster anti-mouse CD48 (clone HM48-1)	BioLegend	Cat# 103403; RRID: AB_313018
Donkey anti-sheep IgG (H+L) Alexa Fluor 555	ThermoFisher Scientific	Cat# A-21436; RRID: AB_2535857
Mouse anti-mouse CD45.1 (clone A20)	BioLegend	Cat# 110706; RRID: AB_313495
Mouse anti-mouse CD45.2 (clone 104)	BioLegend	Cat# 109805; RRID: AB_313442
Mouse Lineage Antibody Cocktail	BD Pharmingen	Cat# 561317; RRID: AB_10612020
Mouse anti-NeuN (clone A60)	Sigma-Aldrich	Cat# MAB377; RRID: AB_2298772
Rabbit anti-GFAP	BioLegend	Cat# PRB-571C; RRID: AB_2565444
Rabbit anti-Iba1	Wako	Cat# 019-19741; RRID: AB_839504
Rabbit anti-NeuN	Abcam	Cat# ab177487; RRID: AB_2532109
Rabbit monoclonal anti-β-Actin (clone 13E5)	Cell Signaling Technology	Cat# 5125; RRID: AB_1903890
Rabbit polyclonal anti-beta 3 adrenergic receptor	Abcam	Cat# ab94506; RRID: AB_10863818
Rat anti-mouse/human CD11b (clone M1/70)	BioLegend	Cat# 101211; RRID: AB_312794
Rat anti-mouse CD16/CD32 (clone 2.4G2)	BD Pharmingen	Cat# 553142; RRID: AB_394656
Rat anti-mouse CD16/CD32 (clone 93)	BioLegend	Cat# 101305; RRID: AB_312804
Rat anti-mouse CD31 (clone MEC13.3)	BioLegend	Cat# 102510; RRID: AB_312917
Rat anti-mouse CD34 (clone RAM34)	BD Pharmingen	Cat# 562608; RRID: AB_11154576
Rat anti-mouse CD41 (clone MWReg30)	BioLegend	Cat# 133927; RRID: AB_2572131
Rat anti-mouse CD45 (clone 30-F11)	TONBO biosciences	Cat# 60-0451; RRID: AB_2621848
Rat anti-mouse CD117 (c-Kit) (clone 2B8)	BioLegend	Cat# 105811; RRID: AB_313220
Rat anti-mouse CD135 (Flt3) (clone A2F10)	BioLegend	Cat# 135309; RRID: AB_1953264
Rat anti-mouse CD140b (PDGFR-β) (clone APB5)	BioLegend	Cat# 136005; RRID: AB_1953270
Rat anti-mouse CD150 (SLAM) (clone TC15-12F12.2)	BioLegend	Cat# 115925; RRID: AB_10896787
Rat anti-mouse CD206 (MMR) (clone C068C2)	BioLegend	Cat# 141717; RRID: AB_2562232
Rat anti-mouse F4/80 (clone BM8)	BioLegend	Cat# 123116; RRID: AB_893481
Rat anti-mouse Ly-6A/E (Sca-1) (clone D7)	BioLegend	Cat# 108107; RRID: AB_313344
Rat anti-mouse Ly-6C (clone HK1.4)	BioLegend	Cat# 128031; RRID: AB_2562177
Rat anti-mouse Ly-6G (clone 1A8)	BioLegend	Cat# 127615; RRID: AB_1877272
Rat anti-mouse TER-119 (clone TER-119)	BioLegend	Cat# 116228; RRID: AB_893636
Bacterial and virus strains		
AAV-Synapsin-GFP (AAV Serotype 8)	SignaGen Laboratories	Cat# SL100838
AAV-Synapsin-Cre-GFP (AAV Serotype 8)	SignaGen Laboratories	Cat# SL100883
Chemicals, peptides, and recombinant proteins		
1,5-Diaminonaphthalene (1,5-DAN)	Sigma-Aldrich	Cat# D21200
2,5-Dihydroxybenzoic acid (2,5-DHB)	Sigma-Aldrich	Cat# 841745
4-(anthracene-9-yl)-2-Fluoro-1-methyl pyridine-1-ium iodide (FMP-10)	Tag-ON	Cat# T1001
7-Chloro-1-methyl-5-phenyl-3H-1,4-benzodiazepine-2(1H)-one (diazepam)	Sigma-Aldrich	Cat# D0899

(Continued on next page)

Continued

REAGENT or RESOURCE	SOURCE	IDENTIFIER
Blocker™ Casein in PBS	ThermoFisher Scientific	Cat# 37582
Cholera Toxin Subunit B (Recombinant), Alexa Fluor™ 594 Conjugate	ThermoFisher Scientific	Cat# C34777
Corn oil	Sigma-Aldrich	Cat# C8267
DAPI Solution	Thermo fisher	Cat# 62248
FD Rapid GolgiStain™ Kit	FD NeuroTechnologies	Cat# PK401
Fluoromount™	Diagnostic BioSystems	Cat# K024
Olive oil	Wako	Cat# 150-00276
OPAL 520 REAGENT PACK	Akoya Biosciences	Cat# FP1487001KT
OPAL 570 REAGENT PACK	Akoya Biosciences	Cat# FP1488001KT
OPAL 690 REAGENT PACK	Akoya Biosciences	Cat# FP1497001KT
RNAscope(R) Multiplex Fluorescent Reagent Kit v2	Advanced Cell Diagnostics, Inc.	Cat# 323100
RNAscope(R) Target Probe-Mm-Gad2-C3, Mouse	Advanced Cell Diagnostics, Inc.	Cat# 439371-C3
RNAscope(R) Target Probe-Mm-Plxna4-C2, Mouse	Advanced Cell Diagnostics, Inc.	Cat# 515491-C2
RNAscope(R) Target Probe-Mm-Rbfox3-C3, Mouse	Advanced Cell Diagnostics, Inc.	Cat# 313311-C3
RNAscope(R) Target Probe-Mm-Sema6d-C1, Mouse	Advanced Cell Diagnostics, Inc.	Cat# 565871
RNAscope(R) Target Probe-Mm-Sema6d-O1-C1, Mouse	Advanced Cell Diagnostics, Inc.	Cat# 1255981-C1
Sodium azide	Wako	Cat# 195-11092
Tamoxifen	Sigma-Aldrich	Cat# T5648
Triton X-100	Nacalai Tesque	Cat# 35501-02
Type I collagenase	Gibco	Cat# 17100017
RIPA Buffer	Nacalai Tesque	Cat# 08714-04
4%-Paraformaldehyde Phosphate Buffer Solution	Nacalai Tesque	Cat# 09154-85
Critical commercial assays		
Chromium Next GEM Single Cell 3' GEM, Library & Gel Bead Kit v3.1	10x Genomics	Cat# 1000128
Chromium Nuclei Isolation Kit with RNase Inhibitor	10x Genomics	Cat# 1000494
LIVE/DEAD™ Fixable Aqua Dead Cell Stain Kit, for 405 nm excitation	Invitrogen	Cat# L34957
LIVE/DEAD™ Fixable Violet Dead Cell Stain Kit, for 405 nm excitation	Invitrogen	Cat# L34955
Myelin removal beads	Miltenyi Biotec	Cat# 130-096-733
Neural Tissue Dissociation Kit (P)	Miltenyi Biotec	Cat# 130-092-628
PowerUp™ SYBR® Green Master Mix	ThermoFisher Scientific	Cat# A25741
QuantiFast Multiplex PCR Kit	Qiagen	Cat# 204757
RNeasy Plus Mini Kit	Qiagen	Cat# 74136
SuperScript® IV Reverse Transcriptase	ThermoFisher Scientific	Cat# 18090010
TruSeq® Stranded mRNA Library Prep	Illumina	Cat# 20020594
Visium Spatial for FFPE Gene Expression Kit, Mouse Transcriptome	10x Genomics	Cat# 1000339
Deposited data		
RNA sequencing data	This paper	GEO: GSE201216
RNA sequencing data	This paper	GEO: GSE195825

Continued

REAGENT or RESOURCE	SOURCE	IDENTIFIER
snRNA sequencing data	This paper	GEO: GSE216431
Preprocessed data of snRNA-seq dataset	This paper	Figshare: https://figshare.com/s/646b50bde8438d8e5ebc
Visium sequencing data	This paper	GEO: GSE220799
Preprocessed data of Visium dataset	This paper	Figshare: https://figshare.com/s/8351aa0ad3bfb1e5f642
Experimental models: Organisms/strains		
Mouse: *Adrb3−/−Sema6d−/−*	This paper	N/A
Mouse: *B6.129(Cg)-Lepr^tm2(cre)Rck^/J*	The Jackson Laboratory	IMSR cat# JAX:008320
Mouse: *B6.Cg-Gt(ROSA)26Sortm6 (CAG-ZsGreen1)Hze/J*	The Jackson Laboratory	IMSR cat# JAX:007906
Mouse: *B6.Cg-Tg(Prrx1-cre)1Cjt/J*	The Jackson Laboratory	IMSR cat# JAX:005584
Mouse: *B6J.B6N(Cg)-Cx3cr1^tm1.1(cre)Jung^/J*	The Jackson Laboratory	IMSR cat# JAX: 025524
Mouse: *B6.SJL-Ptprc^a^ Pepc^b^/BoyJ*	The Jackson Laboratory	IMSR cat# JAX:002014, RRID: IMSR_JAX:002014
Mouse: C57BL/6J	CLEA Japan, Inc.	N/A
Mouse: *Mapt^tm2(cre)Aha^*	Dr. Akihiro Harada (Osaka University, Japan)	Muramatsu et al.[39]
Mouse: *Plxna4−/−*	Dr. Hajime Fujisawa (Nagoya University, Japan) Dr. Fumikazu Suto (National Center of Neurology and Psychiatry, Japan)	Suto et al.[70]
Mouse: *Sema6d^fl/fl^*	This paper	N/A
Mouse: *Sema6d^IRES-Cre/+^*	This paper	N/A
Mouse: *Sema6d−/−*	Our laboratory	Takamatsu et al.[71]
Mouse: *Tg(Cdh5-cre/ERT2)#Ykub*	Dr. Yoshiaki Kubota (Keio University, Japan)	Okabe et al.[72]
Oligonucleotides		
Genotyping primers for *Sema6d^fl/+^* mice	Forward: (5′–3′) CATTGAT GGTCTCATCCTTTCC Reverse: (5′–3′) CACAGAA GAGGAACACAACAAAATG	N/A
Genotyping primers for *Sema6d^IRES-Cre/+^* mice	Forward: (5′–3′) CTGTCAG ACCACTGAACAAGTACAC Reverse: (5′–3′) GTGTAGG AGGATGTTAGTGCTTGTT	N/A
Genotyping primers for *Adrb3+/−* mice	Forward: (5′–3′) TGGCCTC ACAGAAACGGCTCTC Reverse: (5′–3′) TGTTGAG CGGTGGACTCTGCCTG	N/A
M. musculus *Actb*	TaqMan	4352341E
M. musculus *Angpt1*	TaqMan	Mm00456503_m1
M. musculus *Cxcl12*	TaqMan	Mm00445553_m1
M. musculus *Sema6d*	TaqMan	Mm01334446_m1
qPCR primers for M. musculus *Actb*	Forward: (5′–3′) CATTGCTG ACAGGATGCAGAAGG Reverse: (5′–3′) TGCTGGA AGGTGGACAGTGAGG	N/A
qPCR primers for M. musculus *Adrb3*	Forward: (5′–3′) AACTGTG GACGTCAGTGGAC Reverse: (5′–3′) CGTAACG CAAAGGGTTGGTG	N/A

(Continued on next page)

Continued

REAGENT or RESOURCE	SOURCE	IDENTIFIER
sgRNA sequences for targeting M. musculus *Adrb3*	CCATGGGCAGCGGCATT GGC and GCTGGGAAGGT GACTGCGCG	N/A
Software and algorithms		
Fiji (ImageJ)	https://fiji.sc	https://fiji.sc, RRID: SCR_002285
FlowJo	Tree Star	http://www.flowjo.com, RRID: SCR_008520
GraphPad Prism 9	GraphPad	http://www.graphpad.com/, RRID: SCR_002798
ZEN	Zeiss	https://www.zeiss.com/microscopy/us/ products/microscope-software/zen.html, RRID:SCR_013672
SpaceRanger software, v.1.3.0	10x Genomics	https://support.10xgenomics.com
10x Cell Ranger package	10x Genomics	https://support.10xgenomics.com, RRID:SCR_017344
R package Seurat, v.4.0	Hao et al.[73]	https://satijalab.org/seurat/, RRID:SCR_007322
Canek, v.0.2.1	Loza et al.[74]	https://martinloza.github.io/Canek/
CellPhoneDB, v.3.1.0 (database v.4.0)	Garcia-Alonso et al.[50]	https://www.cellphonedb.org/, RRID:SCR_017054
Original code	This paper	DOI: https://doi.org/10.5281/zenodo.12155200, https://github.com/ddiez/Paper_Nakanishi_Sema6d
Other		
Regular Chow Diet	CLEA Japan, Inc.	N/A
HFD32	CLEA Japan, Inc.	N/A

RESOURCE AVAILABILITY

Lead contact
Further information and requests for resources and reagents should be directed to and will be fulfilled by the lead contact, Atsushi Kumanogoh (kumanogo@imed3.med.osaka-u.ac.jp).

Materials availability
Sema6d$^{IRES-Cre/+}$, *Sema6d*$^{fl/fl}$, and *Adrb3*$^{-/-}$*Sema6d*$^{-/-}$ mice are available under an MTA from the authors.

Data and code availability
- RNA-seq data have been deposited at GEO and are publicly available as of the publication date. Accession numbers are listed in the key resources table. Software used for the analyses is described and referenced in the individual method details sub-sections and is listed in the key resources table. Preprocessed data have been deposited on Figshare. The links are listed in the key resources table.
- The code used in the paper has been deposited at Zenodo and is publicly available. The DOI and the link to the latest code in the GitHub repository are listed in the key resource table.
- Any additional information required to reanalyze the data reported in this work paper is available from the lead contact upon request.

EXPERIMENTAL MODEL AND SUBJECT DETAILS

Mice
C57BL/6J mice were purchased from CLEA Japan, Inc. (Tokyo, Japan). *Sema6d*$^{-/-}$ mice were generated as previously described.[71] B6.SJL-*Ptprc*^{a} *Pepc*^{b}/BoyJ (CD45.1, Jax #002014),[75] B6.Cg-Gt(ROSA)26Sortm6(CAG-ZsGreen1)Hze/J (Ai6, Jax #007906),[37] B6.129(Cg)-*Lepr*$^{tm2(cre)Rck}$/J (LepR-Cre, Jax #008320),[40] B6J.B6N(Cg)-*Cx3cr1*$^{tm1.1(cre)Jung}$/J (Cx3cr1-Cre, Jax #025524)[76] and B6.Cg-Tg(Prrx1-cre)1Cjt/J (Prx1-Cre, Jax #005584)[77] mice were obtained from The Jackson Laboratory (Bar Harbor, ME, USA). *Mapt*$^{tm2(cre)Aha}$ (Tau-Cre, MGI #3793311)[39] mice were provided by Dr. Akihiro Harada (Osaka University). Tg(Cdh5-cre/ErT2)#Ykub (VEcad-Cre^{ERT2}, MGI #5705396)[72] mice were provided by Dr. Yoshiaki Kubota (Keio University). *Plxna4*$^{-/-}$ mice were provided by

Dr. Hajime Fujisawa (Nagoya University) with the permission of Dr. Fumikazu Suto (National Center of Neurology and Psychiatry).[70] All mouse strains were congenic with C57BL/6J, except *Plxna4*^{−/−} mice, which were congenic with C57BL/6N. Seven- to twelve-week-old male mice were used, and the experiments were randomized. For BM transplant, 5×10^6 BM cells were intravenously transferred to recipient mice, which were lethally irradiated at a single dose of 10 Gy. Mice were used for experiments at least 12 weeks after reconstitution. Induction of *Sema6d* deletion in *Sema6d*[ΔVEcad] mice was achieved by intraperitoneal injection of tamoxifen (62.5 mg/kg body weight; Sigma-Aldrich, #T5648) dissolved in ethanol (Wako, #057-00456) and corn oil (Sigma-Aldrich, #C8267), for four consecutive days at 7–12 weeks of age. For analysis, littermate controls were used. All the mice used in this study were housed in a pathogen-free facility. All the protocols were approved by the Animal Research Committee of the Immunology Frontier Research Center (Osaka University, Osaka, Japan).

METHOD DETAILS

Generation of Sema6d[IRES-Cre/+] and Sema6d^{fl/+} mice
Major experimental procedures (design and construction of the targeting vector, establishment of targeted embryonic stem cells, generation of chimeric and F1 mice, and removal of *neo* cassette) to generate *Sema6d*[IRES-Cre/+] and *Sema6d*^{fl/+} mice were performed by Unitech, Co. (Kashiwa, Japan). *Sema6d*[IRES-Cre/+] and *Sema6d*^{fl/+} mice were produced from a C57BL/6J genetic background. The founder mice (+/IRES-Cre [neo+] and +/flox [neo+]) were crossed with FLPe transgenic mice to produce *Sema6d*[IRES-Cre/+] and *Sema6d*^{fl/+} mice without the *neo* cassette (+/IRES-Cre [neo-] and +/flox [neo-]). The +/IRES-Cre [neo-] and +/flox [neo-] mice were back-crossed to C57BL/6J mice to remove the FLPe allele. Screening of the mutant mice was performed by PCR with the following primers: forward, 5′-CTGTCAGACCACTGAACAAGTACAC-3′ and reverse: 5′-GTGTAGGAGGATGTTAGTGCTTGTT-3′ for *Sema6d*[IRES-Cre/+] mice; forward, 5′-CATTGATGGTCTCATCCTTTCC-3′ and reverse: 5′-CACAGAAGAGGAACACAACAAAATG-3′) for *Sema6d*^{fl/+} mice. *Sema6d*[IRES-Cre/+] mice express Cre recombinase in SEMA6D-expressing cells, enabling Cre-dependent genetic manipulation.

Generation of *Adrb3*^{−/−}*Sema6d*^{−/−} mice with CRISPR/Cas9
Adrb3^{−/−}*Sema6d*^{−/−} mice were produced by introducing guide RNAs (gRNAs) targeting *Adrb3* with the CAS9 enzyme (Thermo Fisher Scientific) into fertilized *Sema6d*^{−/−} eggs with NEPA21 (Nepagene).[78] A search for single gRNA (sgRNA) and off-target sequences was performed using CRISPRdirect software (https://crispr.dbcls.jp/).[79] The sgRNA sequences used for electroporation were 5′-CCATGGGCAGCGGCATTGGC-3′ and 5′-GCTGGGAAGGTGACTGCGCG-3′ for the second exon of *Adrb3*. Two-cell stage embryos were transferred into the oviducts of pseudopregnant ICR females the next day. Screening of the resulting mutant mice was performed by direct sequencing of PCR products with the following primers: forward: 5′-TGGCCTCACAGAAACGGCTCTC-3′ and reverse: 5′-TGTTGAGCGGTGGACTCTGCCTG-3′ for *Adrb3*^{−/−}.

Genetic correlation and pleiotropic genes
Pairwise genetic correlations of traits in the GWAS atlas, which contains data from 4,756 GWASs across 3,302 unique traits, were computed using LDSC and pleiotropic genes were extracted from MAGMA gene analysis results of traits in the GWAS atlas as described previously.[22] Genetic correlation analysis and extraction of pleiotropic genes were performed among 16 metabolic and 18 psychiatric traits in the GWAS atlas (https://atlas.ctglab.nl/multiGWAS). The value of genetic correlation was winsolized between −1.25 and 1.25. The Bonferroni correction was performed based on the number of possible pair in the heatmap. First genes which were tested in all selected GWAS were selected and considered as genome-wide significant when p < 0.05/the number of tested genes. For each gene, the number of associated GWAS were counted.

Phenotype associations
Phenotypes associated with genetic variants of *SEMA6D* were queried using the GWAS Atlas PheWAS database (https://atlas.ctglab.nl/PheWAS).[22] PheWAS analysis was performed for *SEMA6D* across 4,756 GWASs. Obtained associations were filtered to identify significant traits linked to *SEMA6D* using a Bonferroni-corrected significance threshold ($p < 1.05 \times 10^{-5}$).

In silico analysis of *SEMA6D* expression
To explore whether *SEMA6D* levels differed between patients with schizophrenia and healthy controls, *SEMA6D* data were extracted from the PRJNA379666 dataset.[80]

Open-field test
Mice were gently placed in the center of an open-field arena (50 cm × 50 × 40 cm; W × D × H; gray acrylic walls) and allowed to explore freely for 10 min. A video camera positioned directly above the arena was used to track the movement of each animal, which was recorded on a computer with software (Any-maze; Stoelting) for calculating the total distance and amount of time spent in the center of the chamber compared to the edges. The open-field test is commonly used to measure animals' exploratory behavior and general activity. The test room was dark, the sound was insulated, and the tracking instrument recognized the central body point of the mouse using infrared lasers and sensors. The movements with more time spent on the edges of the box and less time spent in the

center of the box were interpreted as anxiety-like behaviors. Before the test, the mice were acclimatized to the room for 1 h, and the arena was cleaned with 70% ethanol after every trial.

Elevated plus maze test

Mice were introduced into the center quadrant of a four-arm maze with two open arms without walls and two closed arms with walls (30 cm long, 6 cm wide). The structure was elevated 40 cm above the floor. The mice were placed in the center and faced with an open arm at the start of the trial. A video camera positioned directly above the arena was used to track the movement of each animal, which was recorded on a computer with software (Any-maze; Stoelting). The software tracked the time the mice spent in the closed arms versus the open arms throughout a 2.5-minute session. A lower movement frequency in the open arms and less time spent there indicate higher anxiety. Before the test, the mice were acclimatized to the room for 1 h, and the arena was cleaned with 70% ethanol after every trial.

Social interaction test

Mice were kept for 150 s in an open-field chamber (30 cm × 40 cm) with a wire mesh cage (10 cm × 6 cm) enclosing an unfamiliar ICR mouse at one end of the field. Mouse behaviors were video monitored, and the trajectory of mouse ambulation was automatically determined and recorded on a computer using software (Any-maze; Stoelting). A 30 × 15-cm-sized rectangular zone, including the wire mesh cage, was defined as the social interaction zone. A 30 × 9-cm-sized rectangular zone opposite the social interaction zone was defined as the social avoidance zone. The durations spent by each mouse in the respective zones were used as indices for social interaction and avoidance levels, respectively.

Forced swimming test

A forced swimming test was performed in a clear glass cylinder (30 cm height; 19 cm diameter) filled with fresh water (20°C) up to 25 cm from the bottom. The 6-min session was video recorded, and the duration of immobility within this session was calculated offline. Despair behavior was defined as floating without any movement, except for those necessary to keep the nose above water.

Locomotor activity test

Locomotor activity was measured in the home cage (33 × 44 × 32 cm; W × D × H) for 10 min with an infrared sensor on the ceiling (Supermex; Muromachi Kikai).

Rotarod test

Motor coordination and equilibrium were assessed using a rotarod setup (Muromachi Kikai). The mice were trained at a constant speed (4 rpm, 30 s) and then tested. During the test trials, the animals had to balance on a rotating rod that accelerated from 4 rpm to 40 rpm in 300 s, and the latency to fall off the rod was recorded (up to the 5-minute cut-off).

Administration of an anxiolytic drug

7-Chloro-1-methyl-5-phenyl-3H-1,4-benzodiazepine-2(1H)-one (diazepam) was purchased from Sigma-Aldrich (St. Louis, MO, USA), aliquoted on arrival, and diluted in a vehicle (mixture of 10% DMSO and 5% TWEEN 80 in saline) before experiments. Diazepam (2 mg/kg) was intraperitoneally injected into the mice 30 min before behavioral tests.

Stereotaxic microinjection

Mice underwent standard stereotactic procedures with a stereotaxic instrument (Muromachi Kikai). 300 nL of AAV8-hSyn-GFP or AAV8-hSyn-Cre-GFP (2.0 × 10^{13} vg/ml) viruses were injected bilaterally into the CeA (distance from Bregma, AP -1.0 mm, ML ± 3.1 mm, DV -4.95 mm) of at least 8-week-old male $Sema6d^{fl/fl}$ mice using a Hamilton syringe with a 32-gauge needle. Following injections, mice were returned to their home cages. Subsequent experiments were performed in 4 weeks after surgeries. For CTB retrograde tracing, 200 nL of Alexa Fluor 594-conjugated cholera toxin subunit B (5 μg/μL) was unilaterally injected into the CeA. Subsequent experiments were performed in 1 week after surgeries.

Lipid absorption test

Mice were given 9.5 g/kg body weight doses of olive oil (Wako, #150-00276) by oral gavage. Blood samples were collected from tail veins before (basal, time 0) and 1, 2, 3, and 4 h after oral oil administration. Blood samples were centrifuged at 1,000 × g for 15 min at 4°C. After centrifugation, triglyceride concentrations in plasma samples were measured using a gel-permeation high performance liquid chromatography method (LipoSEARCH®; Skylight Biotech, Akita, Japan).[81]

Glucose tolerance test

Fasting blood glucose was measured 20 h after fasting using the Easy Step Blood Glucose Monitoring System. Mice were injected intraperitoneally with glucose at a dose of 1 g/kg body weight. Blood glucose levels were measured 15, 30, 60, and 120 min after the injection.

Flow cytometry

Mouse cells were blocked with anti-CD16/32 (2.4G2) and incubated with the following fluorochrome-conjugated antibodies: anti-CD45.2 (104), anti-CD45.1 (A20), anti-CD11b (M1/70), anti-Ly-6G (1A8), anti-Ly-6C (HK1.4), anti-F4/80 (BM8), anti-CD11c (HL3 or N418), anti-c-Kit (2B8), anti-Sca-1 (E13-161.7 or D7), anti-Flt3 (A2F10), anti-CD48 (HM48-1), anti-CD150 (TC15-12F12.2), anti-CD41 (MWReg30), anti-CD16/32 (93), anti-CD34 (RAM34), anti-TER-119 (TER-119), anti-CD31 (MEC13.3), anti-PDGFR-β (APB5), anti-CD206 (C068C2); a lineage cocktail (Lin) including anti-CD3e (145-2C11), anti-CD11b (M1/70), and anti-B220 (RA3-6B2); anti-TER-119 (TER-119), and anti-Ly-6G and Ly-6C (RB6-8C5). Cells were analyzed with a three-laser, eight-color custom-configuration BD FACSCanto II (BD Biosciences) or sorted with a three-laser, eight-color custom-configuration FACSAria II. All antibodies were purchased from BioLegend (San Diego, CA, USA), eBiosciences, and BD Pharmingen. Dead cells were stained with a live/dead fixable dead cell stain kit (Molecular Probes). Post-acquisition analysis was performed using FlowJo software.

Quantitative PCR

Total RNA was isolated from sorted or fractionated cells using the RNeasy Mini kit (Qiagen), and cDNA was synthesized using SuperScript® IV Reverse Transcriptase (Invitrogen). Quantitative PCR reactions were performed using the QuantiFast Multiplex PCR Kit (Qiagen) or PowerUp™ SYBR® Green Master Mix (Applied Biosystems) and run on a QuantStudio 7 Flex Real-Time PCR System (Applied Biosystems). The following primers were used: *Sema6d* (Mm01334446_m1, Applied Biosystems), *Cxcl12* (Mm00445553_m1, Applied Biosystems), *Angpt1* (Mm00456503_m1, Applied Biosystems), *Adrb3* (forward: 5′-AACTGTGGACGT CAGTGGAC-3′ and reverse: 5′-CGTAACGCAAAGGGTTGGTG-3′), and endogenous control gene *Actb* (forward: 5′-CATTGCTGA CAGGATGCAGAAGG-3′ and reverse: 5′-TGCTGGAAGGTGGACAGTGAGG-3′ for SYBR Green, 4352341E (Applied Biosystems) for TaqMan). Gene expression data were normalized to the expression of *Actb*, which encodes beta-actin.

Histological analysis

Tissues were dissected and fixed in 10% neutral-buffered formalin. Then, paraffin-embedded tissues were sectioned and stained with hematoxylin and eosin (H&E). Microscopic analysis was performed using a Keyence BZ-X800 microscope (Osaka, Japan). Adipocyte size was determined via Adiposoft and ImageJ analyses of H&E-stained tissues, as previously described.[82]

Immunohistochemistry

After deep anesthesia, animals were perfused through the heart with 4% paraformaldehyde (PFA) in phosphate-buffered saline (PBS). The brains were removed from the skull, fixed overnight in 4% PFA, and then dehydrated in 30% sucrose in PBS solution for 72 h until they sunk to the bottom. The brains were rapidly frozen, and coronal brain sections of 30 μm thickness were prepared using a Leica CM3050 S cryostat. After washing with PBS, brain sections were incubated in a blocking buffer composed of PBS containing 0.3% Triton X-100 and 3% bovine serum albumin for 1 h at room temperature (RT). The sections were incubated with appropriate primary antibodies in the blocking buffer at 4°C for 24 h. The primary antibodies used were rabbit anti-Iba-1 (1:1000 dilution), mouse anti-NeuN (1:500 dilution), rabbit anti-NeuN (1:250 dilution), and rabbit anti-GFAP (1:2000 dilution). The sections were washed twice for 10 min at RT in PBS. For immunofluorescence staining, the sections or cells were incubated with Alexa Fluor 488- or 647-labeled secondary antibodies (1:1000 dilution; Life Technologies) for 1 h at RT. The sections were washed twice for 10 min at RT in PBS and stained with DAPI in PBS (1:10000 dilution). Sections were mounted on MAS-coated glass slides (Matsunami Glass) and embedded in FluoromountTM (Diagnostic BioSystems). Imaging was performed using a confocal laser scanning fluorescence microscope (LSM880; Carl Zeiss) with a 63× objective.

Isolation of stromal vascular fractions (SVF) from WAT

Minced white adipose tissue was isolated and digested in PBS with 1.5% bovine serum albumin containing 0.9 mg/mL glucose and 2.5 mg/mL type I collagenase (Gibco, #17100017) for 1 h at 37 °C. Digested tissues were filtered through a 100 μm cell strainer and centrifuged at 190 × *g* for 10 min. The SVF pellets were collected for further analysis.

Isolation of glial cells from the brain

After deep anesthesia, animals were perfused through the heart with PBS. The brains were minced and then enzymatically digested by using Neural Tissue Dissociation Kit P (Miltenyi Biotec) according to the manufacturer's protocol. After the digestion, myelin removal beads (Miltenyi Biotec) were used to removed myelin debris and myelin-bound cell aggregates from single cell suspensions.

Bulk RNA-seq

Library preparation was performed using the TruSeq Stranded mRNA Sample Prep Kit (Illumina, San Diego, CA, USA). Sequencing was performed on an Illumina HiSeq 2500 platform in 75-base single-end mode. CASAVA 1.8.2 software (Illumina) was used for base calling. Sequenced reads were mapped to the mouse reference genome sequence (mm10) using TopHat v2.0.13 in combination with Bowtie2 ver. 2.2.3 and SAMtools ver. 0.1.19. Fragments per kilobase of exon per million mapped fragments (FPKMs) were calculated using Cuffnorm version 2.2.1. Principal components analysis and heatmaps were generated using the R function ggplots2. Gene set enrichment analysis was performed using the Gene set enrichment analysis program.[33]

Visium spatial gene expression library generation

The brains were dissected and fixed in 4% PFA. Paraffin-embedded tissues were sectioned at 5 μm thickness. Brain sections were placed in 6.5 mm-squared capture areas on a Visium Spatial Gene Expression slide (10x Genomics, Inc. Pleasanton, CA, USA), and stored at RT for later use. The spatial gene expression slide was processed according to the manufacturer's protocols. Briefly, tissue sections were deparaffinized and then stained with H&E. Imaging was performed using a Keyence BZ-X710 microscope (Osaka, Japan). Images were stitched together and exported as TIFF files. Following the imaging, the sections were decrosslinked and permeabilized. Reverse transcription and second strand cDNA synthesis was performed. The cDNA was denatured and amplified by PCR to construct sequencing-ready, indexed spatial gene expression libraries. The libraries were sequenced on a NovaSeq6000 (Illumina).

Visium spatial gene expression data processing and analysis

Raw FASTQ files and the histology H&E images were provided as input to the SpaceRanger software (10x Genomics) v.1.3.0. Barcoded spots from four 10x Visium capture areas (WT_1, WT_2, *Sema6d*^{−/−}_1, and *Sema6d*^{−/−}_2) were processed using Seurat v.4.0.[73] Data from the four captured areas were normalized, and the top 5,000 highly variable features were used for batch correction/integration using Canek.[74] The corrected data were scaled and used for principal component analysis (PCA). The top 20 principal components were used to compute UMAP and clusters using the Leiden algorithm[83] with a resolution of 0.6. DEGs between *Sema6d*^{−/−} and WT were calculated for each cluster using FindMarkers. Genes were considered significant with an absolute avg_log$_2$ FC > 0.25 and FDR (p_val_adj) < 0.05. A signature expression was calculated using the scaled sum of *Slc17a7* (*Vglut1*) and *Rspo2* expression for BLA and *Gad2* and *Tac2* expression for CeA to identify BLA and CeA regions of the amygdala. The areas around the amygdala with a strong signal for each signature were manually selected with the shinycluster package (https://github.com/ddiez/shinycluster) and assigned as BLA or CeA. To identify a robust set of markers separating BLA from CeA, differentially expressed genes were calculated between the manually selected BLA and CeA regions using FindMarkers. Genes were considered significant with absolute avg_log$_2$ FC > 1 and FDR < 0.01. Genes with avg_log$_2$ FC > 0 were considered markers for BLA, and those with avg_log$_2$ FC < 0 were for CeA.

In situ RNA hybridization (RNAscope)

RNAscope was performed on fresh frozen coronal brain sections (10 μm thick) using the Multiplex Fluorescence v.2 kits (Advanced Cell Diagnostics) according to the manufacturer's protocol. The probes for mouse *Sema6d*, *Plxna4*, *Gad2* and *Rbfox3* were commercially available from the manufacturer, and the secondary Opal 520, 570, and 690 reagents (FP1487001KT, FP1488001KT, and FP1497001KT, Akoya Biosciences) were diluted with 1:750 in Tyramide Signal Amplification buffer. The sections were then incubated for 5 min in DAPI before being mounted with Fluoromount™ (Diagnostic BioSystems). Imaging was performed using a confocal laser scanning fluorescence microscope (LSM880; Carl Zeiss) with 10×, 20×, and 63× objectives. Analyses of the images were done using ImageJ.

Single-nucleus RNA-seq

Single-nucleus suspensions were isolated from approximately 15 mg of frozen mouse amygdala using a Chromium Nuclei Isolation Kit (10x Genomics), and the nuclear concentration was adjusted to 1000–1200 nuclei/μl. Then, the isolated nuclei were loaded onto a Chromium Next GEM Chip G (10x Genomics) on a Chromium Controller (10x Genomics) for barcoding and cDNA synthesis. The cDNA and library construction were amplified using Chromium Next GEM Single Cell 3' GEM, Library & Gel Bead Kit v3.1, or Chromium Next GEM Single Cell 3' Kit v3.1 (10x Genomics) for 3' profiling according to the manufacturer's protocol. The libraries were sequenced on a NovaSeq6000 (Illumina).

Single nuclei data analysis

Sequenced reads were processed using Cell Ranger (v5.0.0) and aligned with the GRCm38 (mm10) mouse reference genome. Clustering and differential expression analyses were conducted using Seurat v.4.0.[73] The raw data were normalized with NormalizeData. Nuclei with more than 30,000 UMIs, more than 6,000 detected genes, and more than 5% mitochondrial genes were excluded. Several clusters were eliminated as suspicious of containing multiplets based on the co-expression of multiple cell markers. The filtered dataset consisted of 17,656 cells and 21,530 genes. A batch correction was performed with Canek,[74] using the top 5,000 most highly variable features. The corrected data were scaled and used for PCA, and the top 20 principal components were used to calculate UMAP coordinates and clusters with the Leiden algorithm[83] with a resolution of 0.6. The function of "FindAllMarkers" was used to identify cluster-specific genes. Cell clusters were manually annotated as specific cell types based on the literature and datasets for murine cell taxonomy. DEGs between *Sema6d*^{−/−} and WT were calculated for each cluster using FindMarkers with the Wilcoxon Rank Sum test. Genes with an absolute avg_log$_2$ FC > 0.25 and FDR < 0.05 were defined as DEGs. Pathway analyses of DEGs from each cluster were performed using the ingenuity pathway analysis. The list of BLA and CeA markers identified with Visium analysis were used to calculate signature scores with the "AddScoreModules" function to assign cell clusters to either BLA or CeA regions. Cells with a BLA score higher than the CeA score were annotated as BLA and otherwise as CeA.

Cell-cell interaction analysis

The number of ligand–receptor pairs was calculated using CellPhoneDB v3.1.0 (https://www.cellphonedb.org)[50] to infer intercellular communication networks. We applied the method "analysis" using receptors and ligands expressed in at least 10% of the cells in a given cluster. Estimated cell-cell interactions with with $p < 0.05$ were considered significant.

Golgi staining

Freshly dissected mouse brains were processed for Golgi staining, following the manufacturer's protocol (FD Neurotechnologies). Coronal brain sections (250 μm) were generated using a Leica CM3050 S cryostat and placed on gelatin-coated slides overnight. Stained sections were imaged using the 20× and 100× objectives of a Keyence BZ-X800 microscope (Osaka, Japan).

Sholl analysis

BLA pyramidal neurons were reconstructed using the Simple Neurite Tracer (SNT) plugin[84] from ImageJ. Sholl analysis was performed with 5-μm radius interval using SNT. For each experimental group, nine neurons from three mice were analyzed.

Sample preparation for imaging mass spectrometry

The on-tissue derivatization of GABA and glutamate was performed as previously described.[85] In brief, frozen serial 8-μm-thick sections were cut at $-20°$C using a cryostat (CM1950; Leica, Nussloch, Germany) and mounted on indium tin oxide-coated glass slides (100 Ω/sq without adhesive material coating) for matrix-assisted laser desorption/ionization mass spectrometry imaging (MALDI–MSI). The sections were dehydrated in a 50-mL conical tube containing silica gel until derivatization. For GABA detection, the prepared 2-fluoro-1-methyl pyridinium-10 (2.0 mg/1.1 mL in 70% acetonitrile) solution was applied over 1 mL/slide with an airbrush (PS-270, GSI Creos, Tokyo, Japan). For glutamate detection, the prepared 1,5-DAN (7 mg/mL in 70% acetonitrile) solution was applied over 600 μL/slide with the airbrush. The samples were immediately measured after spraying.

MALDI–MSI

MALDI-MSI experiments were performed on a MALDI ion trap time-of-flight mass spectrometer (iMScope TRIO, Shimadzu, Kyoto, Japan) equipped with a 1-kHz Nd:YAG laser ($\lambda = 355$ nm). The laser spot size was approximately 25 μm, and each pixel was irradiated 80–100 times at a repetition rate of 1 kHz. Benzoic acid (2, 5-DHB) was used for m/z calibration. For GABA or glutamate detection, mass spectra were acquired in positive or negative ion detection mode, respectively. The target m/z values of the derivatized neurotransmitters were 371.176 (GABA) and 146.045 (glutamate). The imaging experiment's interval between the data points was 50 or 55 μm in the lateral and axial directions. After sample analysis, ion images were reconstructed, and signal intensities from the region of interest were extracted based on the data using IMAGEREVEAL MS (version 1.21.0.11302, Shimadzu, Kyoto, Japan).

Immunoblotting

Whole-tissue protein lysate was extracted using Qiagen TissueLyser II and RIPA buffer containing 50 mM Tris-HCl (pH 7.6), 150 mM NaCl, 1% Nonidet P-40, 0.5% sodium deoxycholate, 0.1% SDS, and protease inhibitors (Nacalai Tesque, #08714-04). The following antibodies were used in immunoblotting; β-Actin (1:5,000, Cell Signaling Technology, #5125) and β3-AR (1:1,000, Abcam, #ab94506).

QUANTIFICATION AND STATISTICAL ANALYSIS

All statistical analyses were performed using the GraphPad PRISM 9 software. Statistical comparisons between two groups were performed using unpaired two-tailed Student's t-tests or Mann-Whitney test. To compare multiple groups, one-way ANOVA with Dunnett's multiple comparison test, two-way ANOVA with Turkey's multiple comparison test, or two-way repeated-measures ANOVA with Sidak's multiple comparison test was used. Results were considered statistically significant at $p < 0.05$ (*$p < 0.05$, **$p < 0.01$, ***$p < 0.001$, ****$p < 0.0001$, n.s. not significant).